



# Towards Depth-Averaged Modelling of the Decay of Granular Flows by Deposition

Mohammad Nikooei, Clarence Edward Choi<sup>\*</sup>

Department of Civil Engineering, The University of Hong Kong, Pok Fu Lam, Hong Kong SAR, China

## ARTICLE INFO

### Keywords:

Granular flow  
Deposition  
Depth-averaged (DA) models  
2D Smoothed Particle Hydrodynamics (SPH)

## ABSTRACT

Depth-averaged (DA) numerical models are often used to simulate the runout of flow-type landslides because of their practicality and computational efficiency. However, existing DA models generally overlook the effects of deposition, which governs the decay of the flow momentum and the runout distance. In this study, a new approach is proposed to model the effects of deposition. The flow-normal accelerations that drive the deposition process are simulated using a high-fidelity two-dimensional (2D) Smoothed Particle Hydrodynamics (SPH) model. Based on the 2D non-DA SPH results, a deposition model that considers the initial aspect ratio (i.e., height to length) of the debris and slope angle is developed and implemented into the DA context to provide a practical tool for engineering simulations. The new DA SPH model is evaluated against experimental results in the literature. By considering the effects of deposition, predictions of the runout and flow duration are improved by up to 38%. The new DA SPH model works particularly well for runout predictions of large initial aspect ratios of the debris, which has traditionally been the limitation of DA models. The new framework can be used to advance towards realistic deposition and entrainment modelling to improve the delineation of flow-type landslides in mountainous regions.

## 1. Introduction

Numerical models are often used to conduct vulnerability assessments to determine how far a flow-type landslide (Hung et al. 2014), such as granular flows, will travel (Ng et al. 2013) and how much debris will be deposited (Crosta et al. 2009, Edwards and Gray 2015). The momentum and runout of the flows are strongly influenced by the effective flow depth, which is the depth of material over-riding the deposited material. To improve the accuracy of the predictions of the runout and deposited volume, there is a need to reveal the physical basis of the deposition process and model it in a practical and scalable framework for engineering problems.

Deposition occurs when the shear stresses at the boundaries and inside the flow decelerate the debris material, which causes it to come to rest (Crosta et al. 2017, Viroulet et al. 2017). Generally, the deposition process propagates upwards from the channel bed, meaning that there is an interface between the flow and deposited material (i.e., called F/D interface herein) (Zhang and Campbell 1992, Iverson 1997). Capturing the spatial and temporal evolution of the F/D interface is central to modelling the correct physics that govern the deposition process (Doyle

et al. 2007, Lube et al. 2007) and predicting its subsequent events like formation of debris dams (Choi et al. 2018).

Experimental evidence shows that the deposition rate, which is the rate of increase of the depth of the deposited region, can be quantified based on the migration of the F/D interface towards the free surface (Doyle et al. 2007, Lube et al. 2007). Previous studies on the depositional process of flow-type landslides have mainly focused on the morphology and composition of the deposits, including the formation of lateral levees (Iverson 1997, Ghilardi et al. 2001, De Haas et al. 2015, Calvello et al. 2017, Zhou et al. 2019, Baselt et al. 2021). However, less attention has been paid to the investigation of the spatial and temporal variation of the F/D interface as deposition occurs on a slope, which is central to modelling the decay of momentum and improved predictions of the runout and deposited volume.

Practical numerical tools for vulnerability assessments are generally based on depth-averaged (DA) frameworks (Savage and Hutter 1989) because DA models are easy to calibrate and, computationally efficient for field scale simulations (McDougall and Hungr 2004, Pastor et al. 2014, Goodwin and Choi 2022, Su et al. 2022). Over recent years, non-DA models in 2D or 3D have emerged and been used to carry out

<sup>\*</sup> Corresponding author.

E-mail addresses: [MNIKOOEI@HKU.HK](mailto:MNIKOOEI@HKU.HK) (M. Nikooei), [CECHOI@HKU.HK](mailto:CECHOI@HKU.HK) (C.E. Choi).

<https://doi.org/10.1016/j.compgeo.2022.104792>

Received 7 January 2022; Received in revised form 5 April 2022; Accepted 23 April 2022

Available online 17 May 2022

0266-352X/© 2022 Elsevier Ltd. All rights reserved.

numerical back analysis to shed light on the complex dynamics of granular flows (He et al. 2018, Koo et al. 2018, Rauter et al. 2020, Yang et al. 2020). These non-DA models consider the flow-normal accelerations in the flow body and the mass exchange at the F/D interface. Improvements in numerical methods has enabled the underlying physics of erosion and deposition to be simulated (Crosta et al. 2009). 2D or 3D models are more computationally expensive compared to DA models because they require the full-form of the governing equations of the flow to be solved (Ng et al. 2019, Zhou et al. 2019, Yang et al. 2020, Zhou et al. 2020, Bui and Nguyen 2021). Notwithstanding, recent advancements in high performance computing has made substantial progression towards efficient 3D simulations with conventional desktop computers (Peng et al. 2019, Yang et al. 2020, Peng et al. 2022). Evidently, DA models remain favorable for practical engineering problems. However, these models have been reported to overestimate the timescales for the downslope transportation of flow-type landslides by up to two times (Mangeney et al. 2005, Lube et al. 2011). Moreover, it has been reported that DA models fail to replicate the runout measured from experiments of simple collapse of granular material with large initial aspect ratios,  $a$  (i.e., height to length of the column) without the use of unrealistically high friction coefficients (Mangeney et al. 2005, Larrieu et al. 2006, Doyle et al. 2007). The aforementioned limitations of DA models mainly stem from ignoring the accelerations in the flow-normal direction. Consequently, the effects of the evolution of the F/D interface is not explicitly modelled (Edwards and Gray 2015, Edwards et al. 2017, Edwards et al. 2021). In fact, in DA models, deposition is generally assumed to be the inverse of erosion and empirical deposition rates are prescribed into the governing equations of the flow as a source term (Iverson 2012, Pudasaini and Fischer 2020). Empirical deposition rates have limited generalizability and may only be relevant for a specific catchment or event. As an alternative to conventional DA models, multi-layer DA models have also been proposed to replicate the changes in the flow-normal velocity profiles (Sarno et al. 2014, Fernández-Nieto et al. 2018). In the simplest type of these multi-layer models, the flow and deposited regions of the debris are modeled using two different layers with different constitutive relations and a closure equation accounting for the mass flux at their interface. However, the multi-layer models require user-defined closure equations and do not consider the physical effects of evolution of the F/D interface that is observed during the deposition process.

In the DA context, the flow is assumed to have come to rest when the entire block of the granular mass in flow-normal direction is completely stationary (like the stop-and-go mechanism proposed by (Medina et al. 2008)). However, in reality, deposition is a transient process and the granular mass can have simultaneous stationary and flowing regions along the flow path (as will be shown in Section 4.2.1). Therefore, to model the final volume of the flow and its propagation extent properly, the conventional assumptions of DA models should be relaxed and the transient process of deposition should be considered.

In this study, a high-fidelity 2D non-DA Smoothed Particle Hydrodynamics (SPH) method is used to systematically investigate the spatial and temporal variation of the F/D interface of a granular collapse on a slope. Based on the computed results, a deposition model is developed, implemented, and evaluated in the DA framework.

## 2. Smoothed Particle Hydrodynamics (SPH)

### 2.1. Governing equations

Considering the granular mass as an equivalent incompressible continuum, the general conservation equations of mass and momentum are given as follows:

$$\frac{\partial v_x}{\partial x} + \frac{\partial v_y}{\partial y} = 0, \quad (1)$$

and.

$$\frac{\partial v_x}{\partial t} + \frac{\partial(v_x^2)}{\partial x} + \frac{\partial(v_x v_y)}{\partial y} = -\frac{1}{\rho} \left[ \frac{\partial \sigma_x}{\partial x} + \frac{\partial \tau_{yx}}{\partial y} \right] + g_x, \quad (2)$$

$$\frac{\partial v_y}{\partial t} + \frac{\partial(v_y^2)}{\partial y} + \frac{\partial(v_x v_y)}{\partial x} = -\frac{1}{\rho} \left[ \frac{\partial \sigma_y}{\partial y} + \frac{\partial \tau_{xy}}{\partial x} \right] + g_y. \quad (3)$$

where  $v_x$  and  $v_y$  are components of the velocity vector in flow ( $x$ ) and flow-normal ( $y$ ) directions, respectively.  $\sigma_x$  and  $\sigma_y$  are the components of total stress tensor  $\sigma = -pI + \tau$  in  $x$  and  $y$  directions, respectively.  $p$  is the isotropic pressure, and  $I$  is the unit tensor.  $\tau_{yx}$  and  $\tau_{xy}$  are components of the shear stress tensor  $\tau$  in the  $xy$  plane. The density of the equivalent continuum is  $\rho$  and  $g$  is the gravitational acceleration. Well-established constitutive laws such as the viscoplastic and elastoplastic models can reproduce the solid and fluid-like behavior of dense granular flows with reasonable accuracy (Crosta et al. 2009, Ionescu et al. 2015). The 2D non-DA SPH solver in this study adopts a viscoplastic rheological model  $\mu(I)$  (Jop et al. 2006), which is given as follows:

$$\frac{\tau}{p} = \mu(I) \frac{\dot{\gamma}}{|\dot{\gamma}|}, \quad (4)$$

where  $\dot{\gamma}$  is the strain rate tensor. The effective friction coefficient  $\mu(I)$  can be stated as follows:

$$\mu(I) = \mu_s + \frac{\mu_2 - \mu_s}{I_0/I + 1}. \quad (5)$$

where  $I = |\dot{\gamma}|d/\sqrt{p/\rho_s}$  is the inertial number,  $I_0$  is a dimensionless parameter for granular material, which depends on its properties,  $|\dot{\gamma}|$  is the second invariant of the strain rate tensor, and  $d$  and  $\rho_s$  are the diameter and density of the solid particles, respectively. To model the yielding of the equivalent continuum, a Drucker-Prager failure criterion is used (Drucker and Prager 1952).

The full-form of governing equations (1) to (3) are solved using an Incompressible Smoothed Particle Hydrodynamics (ISPH) method (Nikooei and Manzari 2020, Nikooei and Manzari 2021). This ISPH method is based on the work done by (Hosseini et al. 2007) and benefits from a computationally efficient wall boundary condition (Fatehi and Manzari 2012, Mamouri et al. 2015). Details of the discretization of the governing equations are discussed in (Nikooei and Manzari 2020, Nikooei and Manzari 2021).

Governing equations (1) to (3) are averaged in the flow-normal direction  $y$  and manipulated by adopting the kinematic boundary condition in the base of flow (McDougall 2006). Therefore, the one-dimensional DA equations for mass and momentum conservation are derived as follows:

$$\frac{\partial h}{\partial t} + \frac{\partial(uh)}{\partial x} = S_D, \quad (6)$$

and

$$\frac{\partial(uh)}{\partial t} + \frac{\partial(u^2h)}{\partial x} = gh\sin\theta - kgh\cos\theta \frac{\partial h}{\partial x} - \frac{\tau_B}{\rho}. \quad (7)$$

where  $u$  is the DA velocity of the flow in direction of motion, which derivation will be discussed in Section 2.2.  $g = 9.81\text{m/s}^2$ ,  $h$  is the effective depth of flowing mass,  $\theta$  is the slope angle, and  $S_D$  is the source term to incorporate the deposition rate (to be discussed below). A frictional rheology is adopted for the basal friction term (i.e.,  $\tau_B = \text{sgn}(u)\xi \tan\phi_B$ ), where  $\xi = \rho gh\cos\theta$  is the normal stress acting at the base of flowing mass. The basal angle of friction  $\phi_B$  is the only parameter that provides resistance to the flow. A cohesionless granular material is assumed. The parameter  $k$  is the earth pressure coefficient (Hutter et al. 1993), which is defined as follows:

$$k = \frac{2}{\cos^2\phi_1} \left\{ 1 - \sqrt{1 - \cos^2\phi_1(1 + \tan^2\theta)} \right\} - 1, \quad \text{for } \frac{\partial u}{\partial x} > 0, \quad (8)$$

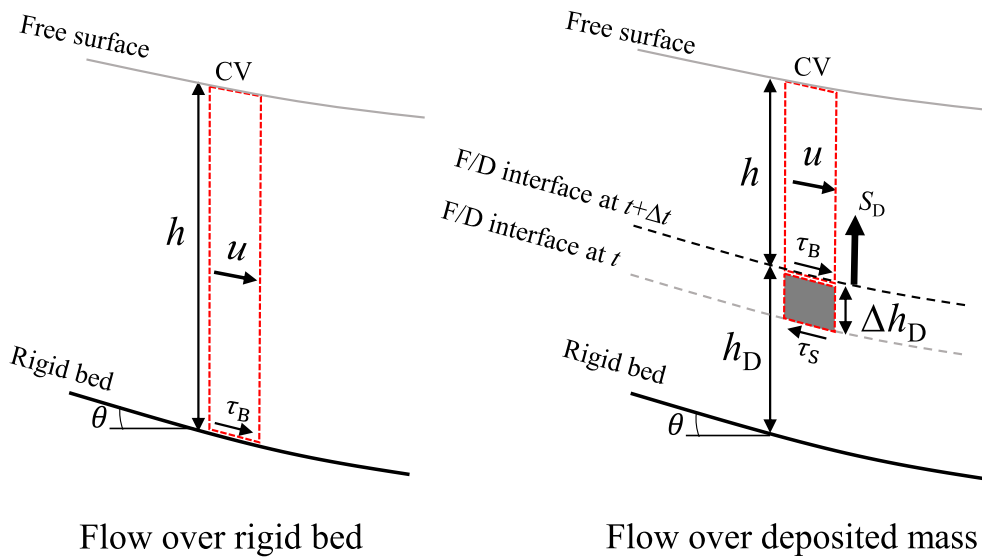


**Fig. 1.** Schematic of a control volume CV of a 1D flowing mass with velocity  $u$  over rigid bed and deposited mass with basal friction  $\tau_B$ . Deposition occurs with the rate of  $S_D$  due to the resistance stress  $\tau_S$ . The change in the depth of the deposited mass in a time step is  $\Delta h_D$ .

and

$$k = \frac{2}{\cos^2\phi_1} \left\{ 1 + \sqrt{1 - \cos^2\phi_1(1 + \tan^2\theta)} \right\} - 1, \quad \text{for } \frac{\partial u}{\partial x} < 0, \quad (9)$$

where  $\phi_1$  is the internal angle of friction of the granular material. Eqns. (6) and (7) can be rearranged as follows:

$$\frac{dh}{dt} + h \frac{\partial u}{\partial x} = S_D, \quad (10)$$

and

$$h \frac{du}{dt} = hg \sin\theta - khg \cos\theta \frac{\partial h}{\partial x} - \frac{\tau_B}{\rho} - uS_D. \quad (11)$$

where the material derivative  $d/dt = \partial/\partial t + u\partial/\partial x$  calculates the temporal and spatial variations in the depth and velocity of the flowing mass. During deposition, a continuous mass loss ( $S_D < 0$ ) from the flowing mass to the deposited region takes place. The mass loss is caused by the shear resistance exerted by the deposited mass. The term  $-uS_D$  on the right-hand side (RHS) of Eq. (11) states that the deposition increases the momentum of the flowing mass. However, for mass flows, deposition occurs during deceleration (to be discussed in Section 4.2.2), which has an arresting effect on it. The source term  $-uS_D$  in the momentum expression stems from the mass exchange between the overlying flow and the underlying deposits. To reproduce the arresting/boosting roles of deposition/erosion on dynamics of flow in a DA framework, a physical interpretation of the deposition and erosion rates and their associated momentum change is needed.

Fig. 1 shows a schematic of basal shear stresses applied on a control volume CV of a one-dimensional flowing mass moves over a rigid bed and a deposited mass. The depth of deposited mass is denoted by  $h_D$ .

When the granular mass flows over a rigid bed, the basal shear stress is expressed as  $\tau_B = \rho g h \cos\theta \tan\phi_B$ . Where  $\phi_B$  is the friction angle between flow particles at the base of flow and a rigid bed (Choi and Goodwin 2021). For a given computational time step  $\Delta t$ , deposition occurs due to the effect of the resistance caused by the internal shear stress (i.e.,  $\tau_S = \rho g \tan\phi_1 (h + \Delta h_D)$ ). Consequently, the part of the flowing mass, with depth  $\Delta h_D$  (i.e., the shaded region), will decelerate from velocity  $u$  to rest on the deposited layer.  $\phi_1$  is the internal friction angle, which differs from the basal friction angle  $\phi_B$ , due to the different composition, strength and interaction forces of materials in bulk of flow and near the bed (Hungry 1995). The overlying flow mass induces a basal

shear stress  $\tau_B = \rho g h \cos\theta \tan\phi_1$  on the deposited mass during deposition. Therefore, the change in momentum ( $uS_D$ ) of the deposited mass with depth  $\Delta h_D$  can be expressed using Newton's second law of motion as follows:

$$uS_D = \frac{\tau_S - \tau_B}{\rho} = g(\Delta h_D) \tan\phi_1. \quad (12)$$

Although one may try to derive the deposition rate  $S_D$  from Eq. (12), this equation is not intended to calculate  $S_D$ , but instead calculates the change in the momentum  $uS_D$  due to the increment in the depth of deposited layer (i.e.,  $\Delta h_D = S_D \Delta t$ ). The calculation of the  $S_D$  will be discussed in the Section 2.2. By substituting Eq. (12) into Eq. (11), the effect of deposition in decreasing the momentum of flow can be recreated.

Although, a simple frictional basal rheology has been widely used in the practical DA analyses such as flowing over complex basal topographies (Gray et al. 1999, Ionescu 2013) and also interaction with obstacles (Cui et al. 2007, Cui and Gray 2013), its benefit in this study is that it offers a simplified relation to describe the change in momentum (Eq. (12)). More importantly, a frictional resistance model does not include high-order viscous terms, which helps to simplify the problem with less input parameters compared to rate-dependent rheological models (e.g.,  $\mu(I)$  rheology (Gray and Edwards 2014)). In addition, the evolution of the F/D interface and deposition process are related to the gradient in the flow-normal direction of the velocity at the interface. The DA model is not able to recover the time and space variation of the velocity profile. Therefore, it can be inferred that the complexity of the basal rheology has a negligible effect on the evolution of the F/D interface and deposition process in flow-normal direction.

## 2.2. Deposition rate and F/D interface

In the DA context,  $hu$  is the momentum flux of the flow and is called DA momentum herein. The time derivative of the DA momentum, can be rewritten using partial derivatives as follows:

$$\frac{d(hu)}{dt} = h \frac{du}{dt} + u \frac{dh}{dt} \quad (13)$$

The inertial term  $hdu/dt$  on the RHS of Eq. (13) includes the temporal variations in the DA velocity  $u$  (i.e., acceleration). The term  $udh/dt$  on the RHS includes the temporal variation in the depth of the flowing mass  $h$  (i.e., deposition rate). Here it is assumed that the term  $udh/dt$  is a ratio

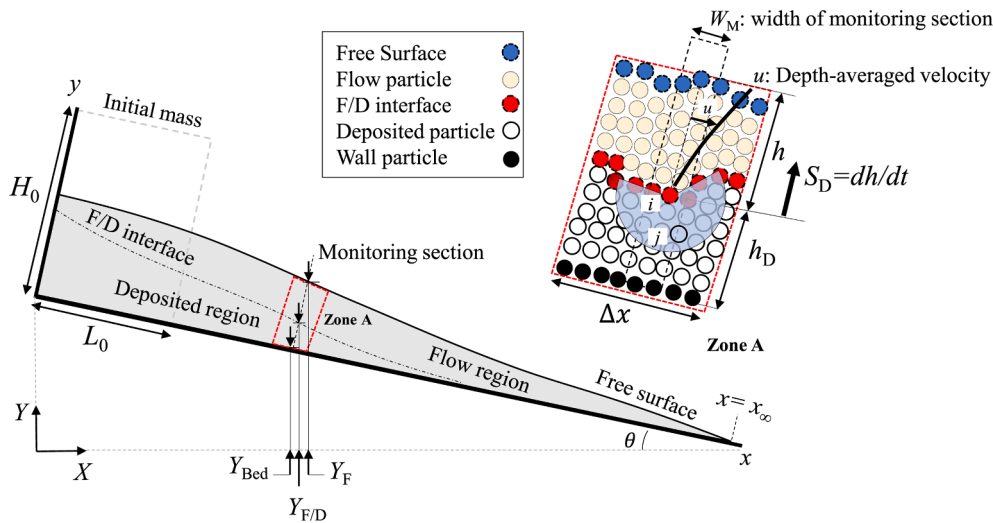


**Fig. 2.** Schematic diagram showing a granular mass with flow and deposited regions as well as the F/D interface. The monitoring section with width of  $W_M$  is used in the 2D non-DA SPH model to calculate the depth-averaged parameters  $h$  and  $u$ . The deposited SPH particles located within the shaded region (e.g. particle  $j$ ) are used to detect SPH particle  $i$  on the F/D interface.

of the time derivative of the DA momentum  $d(hu)/dt$ . Therefore, the deposition rate can be simplified as follows:

$$S_D = \frac{dh}{dt} = \frac{\alpha}{u} \frac{d(hu)}{dt} \quad (14)$$

where  $0 \leq \alpha \leq 1$  is a parameter that governs the deposition process (to be discussed below in Section 4.2.2). This kind of treatment was also adopted by (Rauter and Köhler 2020). For small values of  $\alpha$  (i.e., close to zero) the inertial term  $hdu/dt$  in Eq. (13) governs the change in DA momentum and for large values of  $\alpha$  (i.e., close to one), the change in momentum is mainly caused by the reduction in depth of flowing mass during deposition (i.e.,  $dh/dt$ ). In addition, the effect of changes in velocity on the flow depth is considered by the material derivative  $d(hu)/dt$ .

To analyse the deposition process of a granular mass and obtain a DA version of the deposition rate, the 2D non-DA SPH model is used (Nikooei and Manzari 2020, Nikooei and Manzari 2021). Fig. 2 shows a typical granular mass with a F/D interface in continuum scale. The total depth of the flow  $h_T = h + h_D$  is the summation of the effective depth of flowing mass and the depth of deposited mass. The final runout of the flow is  $x_\infty$ . It is assumed that during deposition the flow is shallow (i.e.,  $h_T/x_\infty \ll 1$ ) and variations in the total depth of the flow is small so that the deposition rate can be defined as  $S_D = -dh_D/dt = dh/dt$ . In Section 4.2.1, it will be shown that during deposition, the total depth of granular mass is nearly constant and the assumption of  $S_D = -dh_D/dt = dh/dt$  is proven to be a reasonable one.

In Fig. 2, the initial aspect ratio of the granular column is defined as  $a = H_0/L_0$ . Decay and growth of flow momentum during the deposition and erosion, respectively, depend on the location and displacement of the granular particles along the flow path (McDougall and Hungr 2005). Analysing the internal dynamics of a flow using monitoring sections in specified locations (i.e. Eulerian approach) enables location-based deposition and erosion models to be obtained. So, in this paper, the monitoring sections at specified locations are intended to capture the spatial and temporal changes of the F/D interface and calculate the deposition rate of the flow material.

In the 2D non-DA SPH model, the depth-averaged velocity at a specified monitoring section is given as follows:

$$u = \frac{\sum_{m=1}^{N_M} (v_x)_m}{N_M} \quad (15)$$

where  $N_M$  is the number of SPH particles crossing the monitoring section

with width of  $W_M$ , and  $v_x$  is the velocity of SPH particles in direction of the slope.  $W_M$  is set to be two times the initial distance between SPH particles (i.e., 0.004 m). The sensitivity of the results to the value of  $W_M$  is discussed in the Appendix.

To calculate the deposition rate, information on the spatial and temporal location of the F/D interface is needed. The particle-based nature of the SPH method enables the dynamics of the F/D interface to be computed. The SPH particles of the flow and deposition regions as well as the particles at the interface is shown on the inset.

The F/D interface is not a physical boundary and has a zone of transition, which can be observed in the velocity profile of the granular mass where the velocity exponentially decays from non-zero values in flowing region to zero values in deposited region (Forterre and Pouliquen 2008, Mangeney et al. 2010, Farin et al. 2014). To identify these two regions and find the location of the F/D interface for calculation of the deposition rate, a critical value for the velocity can be used (Mangeney et al. 2007, Farin et al. 2014). Experimental observations report that at velocities lower than the critical value, the frictional stresses between particles increase and come to rest (Lube et al. 2007). This critical value can be justified using image analysis and calculating the intensity difference between two consecutive images from the transition zone. Different particle characteristic (e.g. diameter) can change the critical velocity and eventually the position of the F/D interface (Lajeunesse et al. 2005). In this paper, a critical value of 0.1 m/s is adopted based on the experimental data (Lube et al. 2007) used to evaluate the computed results. This critical velocity determines whether the SPH particles are part of the flow or deposition.

A F/D particle at the interface denoted as  $i$  is identified using the divergence of the position vector  $\nabla \cdot \mathbf{r}$  as follows:

$$(\nabla \cdot \mathbf{r})_i = \sum_{j=1}^{N_D} (m_j/\rho_j) r_{ij} \nabla W_{ij} \quad (16)$$

where  $N_D$  is the number of deposited particles surrounding an arbitrary particle  $i$  (e.g., particle  $j$  is within shaded region).  $m_j/\rho_j$  is the ratio between the mass and density of neighboring particles. The distance vector between particles  $i$  and  $j$  is denoted as  $r_{ij}$ .  $W_{ij}$  refers to the kernel function and has a non-zero value for particles that are within the supporting domain of the particle  $i$ . In 2D non-DA SPH model, the supporting domain is a circular region with a radius equivalent to smoothing length around SPH particle  $i$ . More details about the kernel function and smoothing length of 2D SPH is available in (Monaghan 1992).

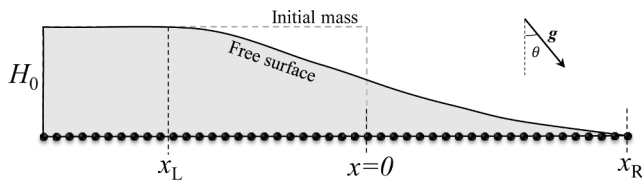


Fig. 3. Schematic of a one-dimensional DA SPH method. The collapse of granular mass occurs at  $x = 0$  and the depth of flow extends from  $x_L$  to the front location  $x_R$ .

(Lee et al. 2008) proposed Eq. (16), which is used to track the free surface particles in the SPH method. Similarly, this equation can be adopted to identify the F/D interface particles. The supporting domain of the SPH particles that fall entirely within the deposited region contains only the deposited SPH particles (i.e., full kernel support). Thus,  $\nabla \cdot r$  is approximately equal to two. For the particles that are on the F/D interface, there is a deficiency of neighboring deposited particles at their supporting domain (shaded region in inset) and the value of  $\nabla \cdot r$  decreases from two. Thus, a threshold value for  $\nabla \cdot r$  can be used to detect particles of the F/D interface. In this study, a threshold value of 1.6 was selected to detect the particles at the F/D interface. Threshold values that are larger and smaller than 1.6 will result in the detection of an interface that has more than a single layer of particles or no F/D interface layer will be detected, respectively.

After the F/D interface particles are detected, the effective depth of the flowing mass and depth of deposited mass can be calculated as follows:

$$h = \frac{Y_F - Y_{F/D}}{\cos\theta}, \quad h_D = \frac{Y_{F/D} - Y_{Bed}}{\cos\theta}. \quad (17)$$

where  $Y_F$ ,  $Y_{F/D}$ , and  $Y_{Bed}$  are the vertical locations of the free surface, F/D particles, and the base of granular mass, respectively, following a coordinate system where  $X$  is the horizontal direction and  $Y$  is the vertical direction.

### 2.3. Depth-averaged SPH model

To study the effects of deposition in the DA context, a depth-averaged and one-dimensional SPH code (hereafter called as DA SPH) is developed. Fig. 3 shows the SPH particles along a horizontal line considered as part of the computational domain in the DA SPH model. In the 2D non-DA SPH model, however, the SPH particles in computational domain are considered in plane (Fig. 2). After the collapse of the initial mass at  $x = 0$ , the free surface of the collapsed mass forms between locations  $x_L$  and  $x_R$ . At  $x \leq x_L$  the flow depth is  $h = H_0$ ,  $x_R$  is the front of the flow and the flow depth is  $h = 0$  for  $x \geq x_R$ .

The values of depth and volume ( $V$ ) are assigned to each SPH particle. The approximation of any variable  $A(x_i)$  and its gradient  $\nabla A(x_i)$  for particle  $i$  can be obtained as follows:

$$A(x_i) = \sum_{j=1}^N V_j \frac{A(x_j)}{h_j} W(x_i - x_j, L_s). \quad (18)$$

$$\nabla A(x_i) = \sum_{j=1}^N V_j \frac{A(x_j)}{h_j} \nabla W(x_i - x_j, L_s). \quad (19)$$

where  $L_s$  is the smoothing length in DA SPH in which the kernel function  $W_{ij}^{DA} = W(x_i - x_j, L_s)$  has a non-zero value.  $N$  is the total number of SPH particles in supporting domain of particle  $i$ . The depth of the flowing mass  $h(x_i)$  and its gradient  $\nabla h(x_i)$  for any specific particle  $i$  can be approximated by considering  $A(x) = h$  as follows:

$$h(x_i) = \sum_{j=1}^N V_j W_{ij}^{DA}, \quad (20)$$

$$\frac{\partial h}{\partial x}(x_i) = \sum_{j=1}^N V_j (B_1)_i \nabla W_{ij}^{DA}. \quad (21)$$

where

$$(B_1)_i = - \left[ \sum_{j=1}^N \frac{V_j}{h_j} W_{ij}^{DA} \right]^{-1}. \quad (22)$$

$(B_1)_i$  is the renormalization factor that improves the interpolation near the initial and final boundaries of the computational domain where there is a deficiency of neighboring particles in the supporting domain of particle  $i$ . It has been shown that the Gaussian kernel function (Gingold and Monaghan 1977) offers improved computational accuracy (Hongbin and Xin 2005), enhanced stability (Morris 1996), and lower computational cost (Colagrossi 2005) among the different types of kernel functions in the literature. Therefore, the adopted Gaussian kernel function and its gradient are defined as:

$$W_{ij}^{DA} = \frac{1}{L_s \sqrt{\pi}} e^{-((x_i - x_j)^2 / L_s^2)}, \quad (23)$$

$$\nabla W_{ij}^{DA} = \frac{2(x_i - x_j)}{L_s^3 \sqrt{\pi}} e^{-((x_i - x_j)^2 / L_s^2)}. \quad (24)$$

Because of the large deformations in the SPH particle sets, the smoothing length will be updated at each time step  $\Delta t$  to consider an approximately constant number of neighboring particles to ensure a smooth interpolation. As such, a variable smoothing length is adopted (Monaghan 1985):

$$L_s = \frac{B N_T}{\sum_{i=1}^{N_T} \frac{h_i}{V_i}} \quad (25)$$

where  $B$  is a constant that governs the number of neighboring particles.  $N_T$  is the total number of SPH particles in the computational domain. In this paper,  $B = 50$  and the kernel value diminishes when  $|x_i - x_j| / L_s \geq 2$ . For larger values of  $B$ , smoothing will be carried out using an unrealistic large value of neighboring particles and the accuracy will decrease. Smaller values of  $B$  will result in less accurate interpolation and cause computational instability in the front of flow, where the velocity has its largest value and the SPH particles move away from each other.

### 2.4. Time integration scheme

The discretized form of governing equations (10) and (11) in SPH are written as follows:

$$h_i^{n+1} = h_i^n - h_i^n \left( \left( \frac{\partial u}{\partial x} \right)_i^n + (S_D)_i^n \right) \Delta t, \quad (26)$$

and.

$$a_i^{n+1} = g \sin\theta - k g \cos\theta \left( \frac{\partial h}{\partial x} \right)_i^{n+1} + \left( \frac{\tau_B}{\rho h} \right)_i^{n+1} - \left( \frac{u S_D}{h} \right)_i^{n+1}. \quad (27)$$

where  $a = du/dt$  is the acceleration. The flux term  $\partial u / \partial x$  on the RHS of Eq. (26) is calculated by using an alternative symmetrized form of Eq. (19) (Randles and Libersky 1996):

$$\frac{\partial u}{\partial x} = \sum_{j=1}^N V_j (u_j - u_i) (B_2)_i \nabla W_{ij}^{DA}, \quad (28)$$

$$(B_2)_i = - \left[ \sum_{j=1}^N V_j (x_j - x_i) \nabla W_{ij}^{DA} \right]^{-1}. \quad (29)$$

where  $(B_2)_i$  is the renormalization factor. In the present DA SPH solver, the smoothing length is updated using Eq. (25) at each time step. Based

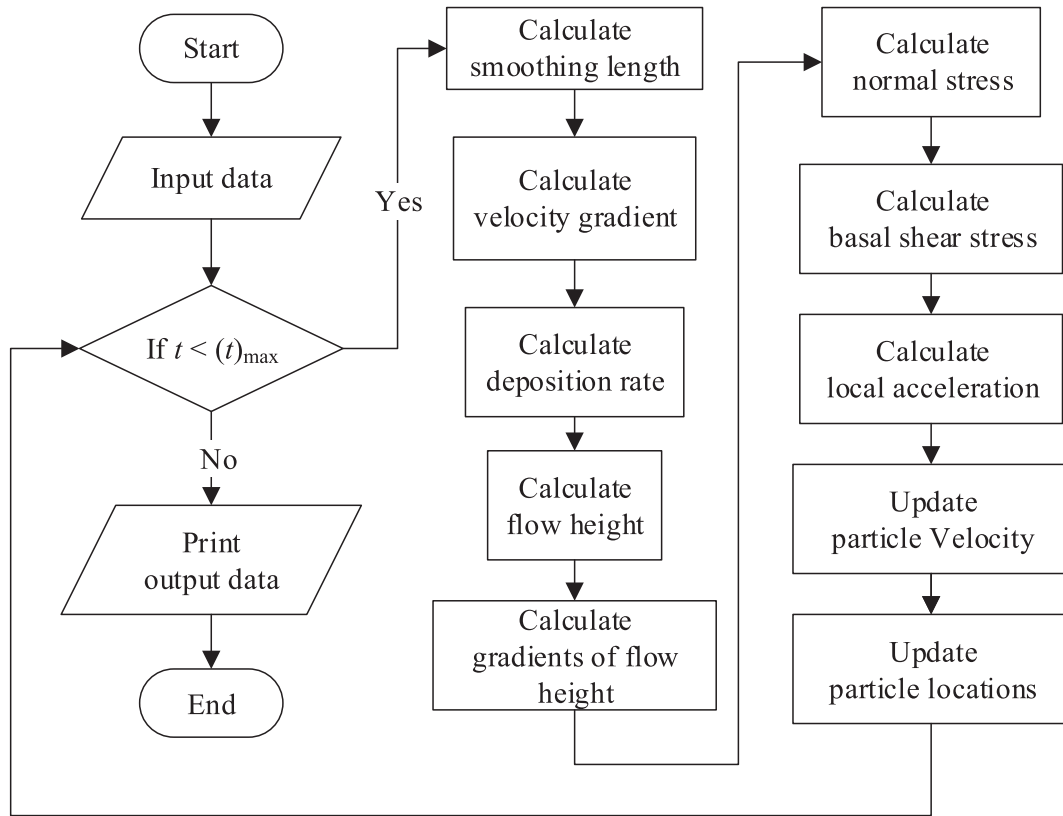


Fig. 4. Algorithm of the DA SPH model.

Table 1

Simulation cases for studying the effects of the initial aspect ratio  $a$  and inclination angle  $\theta$  on deposition. The initial length of granular column is  $L_0 = 0.2\text{ m}$ .

Case ID	$\theta$	$H_0(\text{m})$	$a$	Case ID	$\theta$	$H_0(\text{m})$	$a$
T10-A35	10°	0.07	0.35	T10-A100	10°	0.2	1
T16-A35	16°			T16-A100	16°		
T22-A35	22°			T22-A100	22°		
T16-A50	16°	0.1	0.5	T10-A120	10°	0.24	1.2
T22-A50	22°			T16-A120	16°		
T10-A70	10°	0.14	0.7	T22-A120	22°		
T22-A70	22°			T22-A150	22°	0.3	1.5

on the information from the previous time step and an approximation of the convection term (Eq. (28)), the effective depth of flow in the updated time step  $n + 1$  is calculated by using Eq. (26). This updated value of depth of the flowing mass is used to calculate the pressure term  $\partial h/\partial x$  and the normal and basal stresses. The deposition rate in Eqns. (26) and (27) is obtained using Eq. (14). The 2D non-DA SPH simulations are not performed in parallel with the DA model, but are performed to find the generalized relation for the parameter  $\alpha$  in Eq. (14) (details are discussed in Section 4.2.2). After the calculation of the acceleration in time step  $n + 1$ , the velocity and position of DA SPH particles are updated using the second-order Runge–Kutta method:

$$u_i^{n+1} = u_i^n + \frac{\Delta t}{2} (a_i^{n+1} + a_i^n), \quad (30)$$

and.

$$x_i^{n+1} = x_i^n + \frac{\Delta t}{2} (u_i^{n+1} + u_i^n). \quad (31)$$

A summary of the algorithm of the DA SPH method is shown in Fig. 4. A variable time step method is used:

$$\Delta t = \text{CFL} \times \min \left\{ \frac{L_s}{\max(|u_i|, \sqrt{gh_i})} \right\}. \quad (32)$$

Here, the Courant–Friedrichs–Lewy (CFL) coefficient has a value of  $0 < \text{CFL} \leq 1$  to stabilize the numerical simulation. To avoid tensile instability, which causes the SPH particles to cluster, the XSPH method is used (Monaghan 2000). In the XSPH, the velocity of SPH particles (Eq. (30)) is corrected by the following expression:

$$(u_i^{n+1})_{\text{Corrected}} = u_i^{n+1} + \delta \left[ \sum_{j=1}^N \frac{2V_j}{(h_i + h_j)} (u_j - u_i) W_{ij}^{\text{DA}} \right]. \quad (33)$$

By adopting  $\delta = 0.05$ , a smooth approximation the of velocity and depth of flowing mass are obtained.

### 3. Model setup and parameters

The collapse of a granular column on an inclined plane is considered a fundamental benchmark for the evaluation of numerical models because it encapsulates the dynamics of granular flows during the initiation, propagation and deposition (Mangeney et al. 2010, Lube et al. 2011, Farin et al. 2014). To simplify the simulation conditions, the initial length of granular column is kept constant as 0.2 m and only the initial height is varied to obtain different initial aspect ratios. Deposition occurs when the slope angle is smaller than the friction angle ( $\theta < 25.5^\circ$ ), so three different values of  $\theta = 10^\circ, 16^\circ$  and  $22^\circ$  are simulated. A summary of the simulation plan is given in Table 1. In the case ID T10\_A35, 10 indicates the slope and the 35 refers to the initial aspect ratio  $a$ .

For each simulation case, a total of eleven monitoring sections are located at equal distances apart. The location of each section is selected based on the computed final runout distance  $x_\infty$ , which is defined in Fig. 2. The first and last monitoring sections are located at  $x = L_0$  and  $x = x_\infty$ , respectively. The normalized location of monitoring sections (i.

**Table 2**

Properties of the granular materials used in experiments (Lube et al. 2007, Mangeney et al. 2010) adopted for verification of the present 2D non-DA SPH model.

Material type	Particle diameter $d$ (mm)	Particle density $\rho_s$ (kg/m <sup>3</sup> )	Volume fraction of granular particles	Bulk density $\rho$ (kg/m <sup>3</sup> )	Friction angle $\phi_i$
Glass beads	0.7	2500	0.62	1550	25.5°
Quartz sands	1.5	2600	0.55	1430	31°

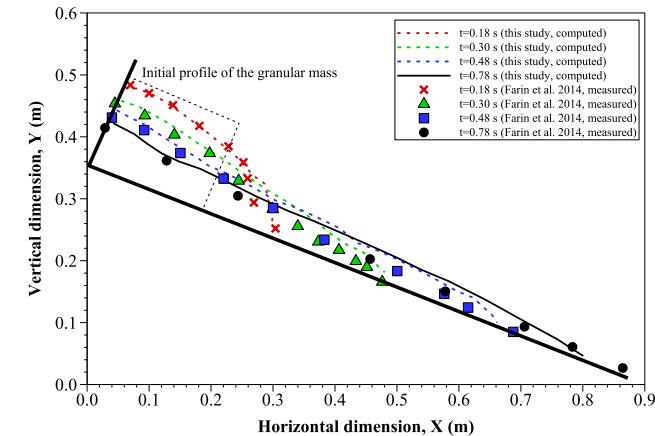


**Fig. 5.** Comparison of measured (Farin et al. 2014) and computed (2D non-DA SPH) free surface for a column collapse on a slope (test case T22-A70).

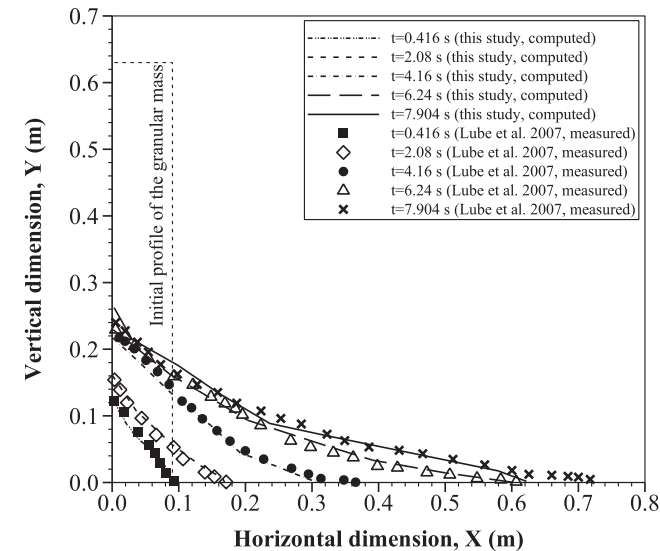


**Fig. 6.** Comparison of measured (Lube et al. 2007) and computed (2D non-DA SPH) F/D interfaces of granular material collapsing on a horizontal plane.

e.,  $[x_M] = (x_M - L_0)/(x_\infty - L_0)$  is used in the interpretation of the results. At each monitoring section, the location of the F/D interface particles and the depth of deposited mass are calculated using the 2D non-DA SPH method discussed in Section 2.2.

The experimental data obtained by (Farin et al. 2014) and (Lube et al. 2007) are used to evaluate the simulation results of granular flow over inclined planes and the presented method for the computing the F/D interface, respectively. The properties of the granular materials used

in their experiments are given in Table 2.

The bulk density of the Quartz sand was not reported in (Lube et al. 2007), therefore, it is calculated by assuming a volume fraction of 0.55 and the reported particle density as follows  $\rho = 2600 \times 0.55 = 1430 \text{ kg/m}^3$ , which is a reasonable estimation based on comparison with similar data (Yan and Wen 2020). The values of  $\mu_s = \tan(\phi_1)$ ,  $\mu_s \approx 0.73$  and  $I_0 = 0.279$  are selected (Ionescu et al. 2015). The values of the particle diameter, density, and friction angle that are used for the rheological model (Eq. (4)) in the 2D non-DA SPH simulations is summarized in Table 2.

#### 4. Interpretation of results and discussion

##### 4.1. Verification of the non-DA numerical results

To evaluate the 2D non-DA SPH model, a comparison between measured and computed results are shown in Fig. 5 and Fig. 6. The computed free surface profile of flow over an inclined plane is compared with measured data reported by (Farin et al. 2014) in Fig. 5.

The granular mass with the initial aspect ratio 0.7 collapses over an inclined rigid plane with  $\theta = 22^\circ$ . The computed free surfaces of the flow using 2D non-DA SPH at different times are compared with the observed one in the experiments. The numerical results are generally in good agreement with the experiments. However, at  $t = 0.78 \text{ s}$ , the numerical solver slightly underestimates the runout. The discrepancy may be caused by an insufficient number of SPH particles at the front of the flow and can be addressed by increasing the number of SPH particles. In addition, experiments generally exhibit scattered granular particles at the front of the deposit, which may cause discrepancies when identifying the extent of the runout (Dufresne 2012). Furthermore, in the numerical modeling of dense granular flows using continuum approaches like the SPH, the no-slip boundary condition cannot easily replicate the behavior of the flow close to rigid boundaries (Savage and Dai 1993, Artoni and Santomaso 2014). Therefore, the present SPH solver is implemented with a slip velocity, which can predict the propagation of the granular mass with more accuracy (Nikooei and Manzari 2020). This slip velocity is calculated based on the stress field inside the granular mass and is applied to SPH particles close to the rigid boundaries. Without applying the slip velocity to the SPH particles, the runout of flow will be underestimated even at the early stages of flow (Cremonesi et al. 2017).

Fig. 6 shows a comparison of the computed profile of the F/D interface with the measured data reported by (Doyle et al. 2007). The evolution of the F/D interface during the collapse of a Quartz sand with an initial aspect ratio of  $a = 7$  on a horizontal plane is shown.

The profiles of the F/D interface are computed using the method described in Section 2.2. The results are shown for five different times starting from 0.416 s. A comparison of the results show that the calibrated 2D non-DA SPH model can be used for analysing the spatial and temporal variation of the F/D interface during the motion of the granular mass. The granular mass beneath the F/D interface at  $t = 0.416 \text{ s}$  is an undisturbed mass that remains static during the collapse. The profile of F/D interface at  $t = 7.904 \text{ s}$  shows the final deposited profile of the granular mass. During the collapse, the F/D interface moves towards the free surface and eventually causes the granular mass to come to rest. Some discrepancies between the computed and measured profiles of the F/D interface can be seen. These discrepancies may have been caused by the simplifications made in numerical simulations, such as adopting a constant friction angle. The difference in the computed and measured profiles at  $t = 7.904 \text{ s}$  refers to the overestimation of the runout due to the slip velocity that is adopted.

##### 4.2. Extraction of data from 2D non-DA SPH model for DA model

###### 4.2.1. Evolution of the F/D interface

In this section, the computed results from the 2D non-DA SPH model

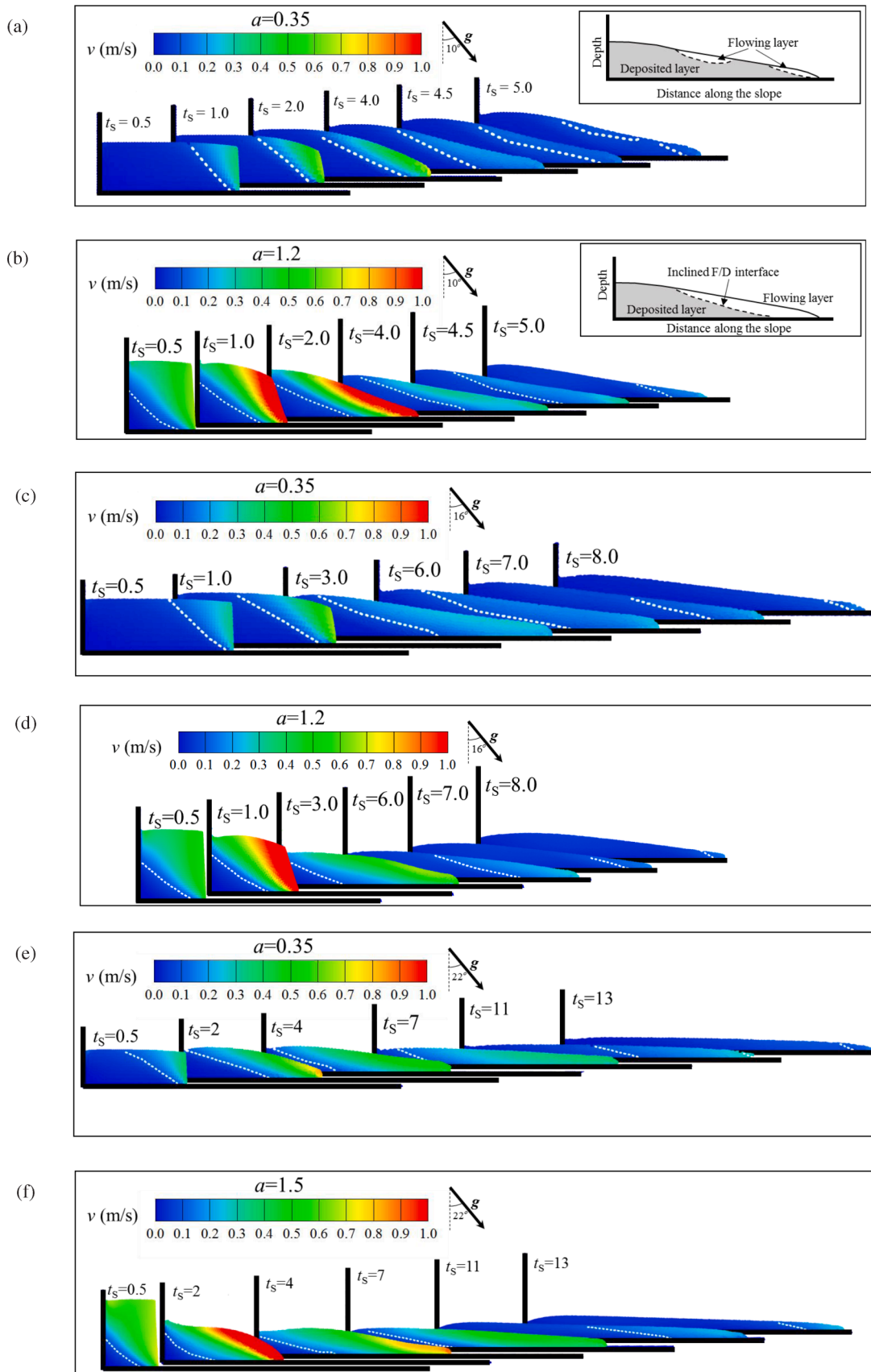


Fig. 7. Temporal evolution of the profiles of the F/D interface (dashed line) for the cases a) T10-A35, b) T10-A120, c) T16-A35, d) T16-A120 e) T22-A35, and f) T22-A150. The results are shown at normalized time  $t_s$ .

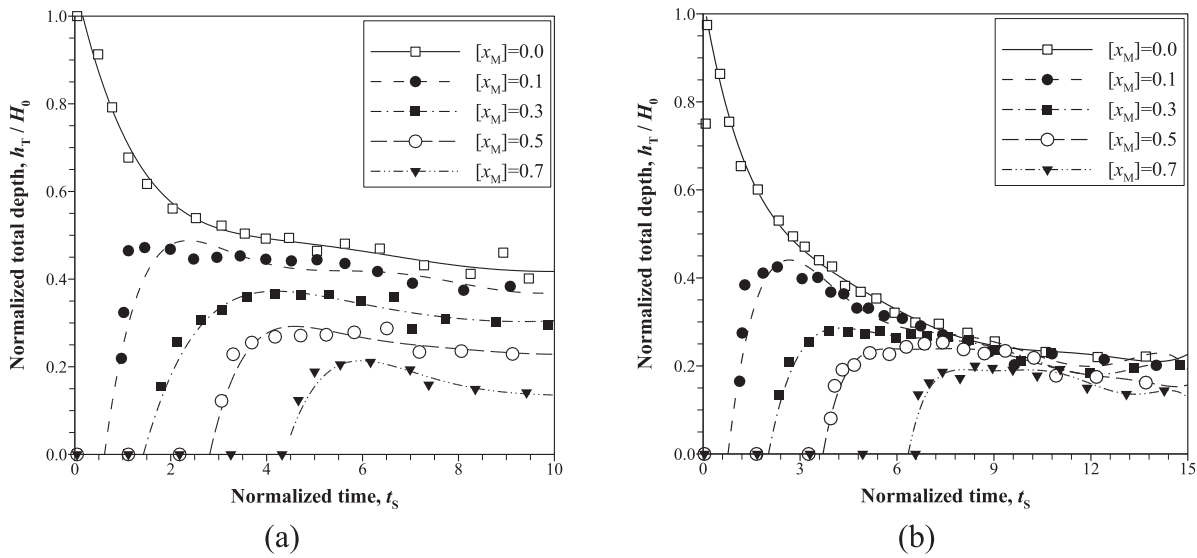


Fig. 8. Computed temporal variations of the normalized total depth of granular mass at different normalized locations along the slope for the cases a) T16-A50, and b) T22-A70.

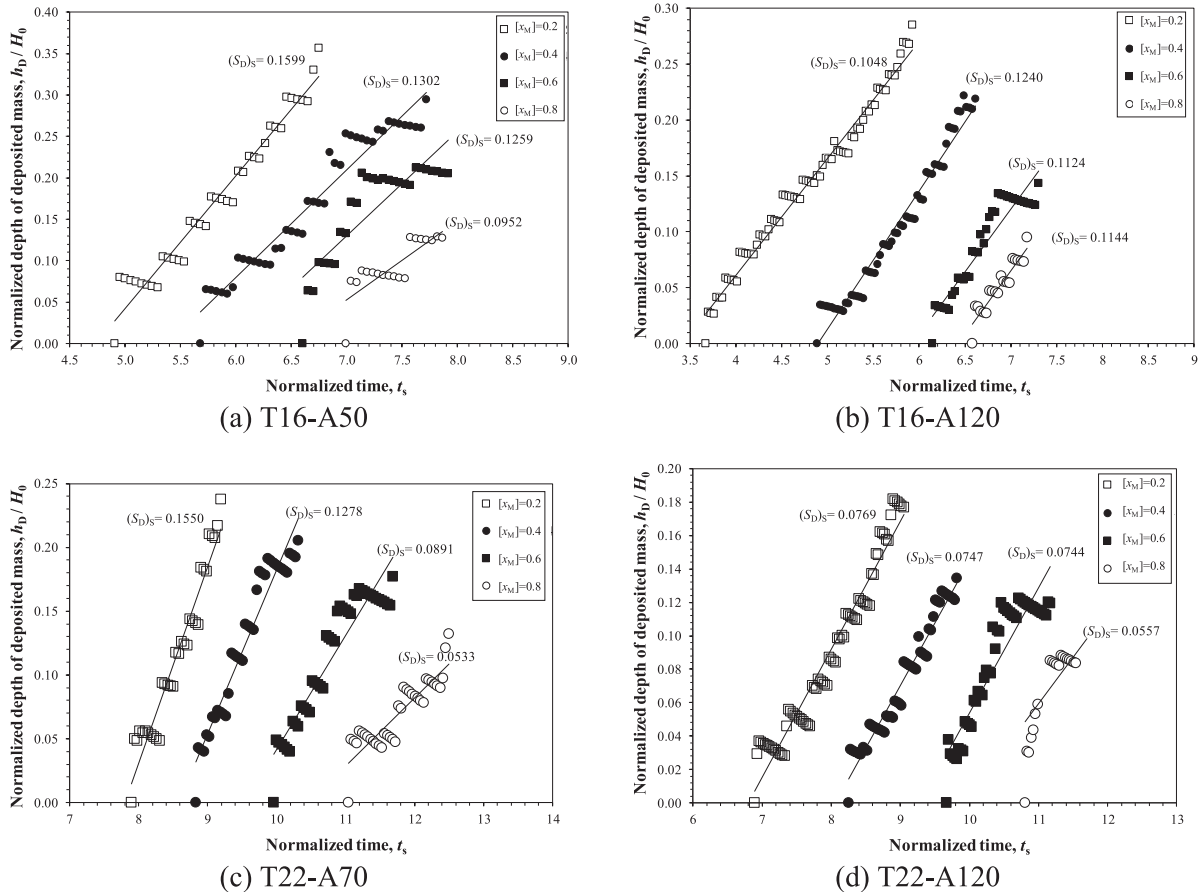


Fig. 9. Computed temporal variations in the normalized depth of deposited mass at different normalized locations along the slope for the cases a) T16-A50, b) T16-A120, c) T22-A70, and d) T22-A120.

are used to track the evolution of the F/D interface and the deposition process is investigated. The evolution of the F/D interface for slope angles of  $\theta = 10^\circ$ ,  $\theta = 16^\circ$ , and  $\theta = 22^\circ$  is shown in the Appendix.

Fig. 7 shows the evolution of the F/D interface for typical cases with  $\theta = 10^\circ$  (T10-A35, T10-A120),  $\theta = 16^\circ$  (T16-A35, T16-A120), and  $\theta =$

$22^\circ$  (T22-A35, T22-A150). The results are shown with dimensionless time  $t_s = t/t_c$ , where  $t_c = \sqrt{H_0/g\cos\theta}$  is the characteristic time scale of flow. The results show the entire evolution of the F/D interface until the flow comes to rest and smaller time increments are shown. The velocity of the flow is calculated as  $v = \sqrt{u_x^2 + u_y^2}$ .

**Table 3**

Calculated normalized critical times for onset of deposition at different locations along the slope for the cases with  $\theta = 16^\circ$  and  $\theta = 22^\circ$ .

Case	Normalized critical time, $(t_s)_C$			
	$[x_M] = 0.2$	$[x_M] = 0.4$	$[x_M] = 0.6$	$[x_M] = 0.8$
T16-A35	5.34	5.92	6.79	7.31
T16-A50	4.90	5.68	6.60	6.99
T16-A100	4.02	5.35	6.24	6.62
T16-A120	3.67	4.89	6.14	6.58
T22-A35	9.29	10.37	11.80	12.14
T22-A50	8.82	9.68	10.63	11.87
T22-A70	7.90	8.83	9.95	11.04
T22-A100	7.86	8.90	9.76	10.58
T22-A120	6.89	8.25	9.67	10.80
T22-A150	5.37	8.15	9.17	9.94

At the initial stages of the collapse, the F/D interface separates the granular mass into flowing and deposited regions. Formation of this initially deposited region governs the initial effective depth and momentum of flowing mass. For small initial aspect ratio, the deposited region resembles a trapezoid, while it has a wedge-like shape for cases with large initial aspect ratio. These two different shapes of the initial deposited mass affects onset of deposition as will be discussed later. For the case with  $a = 0.35$  and  $\theta = 10^\circ$ , the flow comes to rest at  $t_s = 5.5$ . For  $t_s = 5$ , the F/D interface moves towards the free surface and two separated flowing regions develop, one at the middle of the main body and near the free surface, and the other at the front of flow (inset of Fig. 7-a). A similar behavior of the F/D interface has been observed for spreading of the granular mass over shallow and horizontal inclination angles (Crosta et al. 2009). The flowing mass at the middle of the main body does not affect the runout of the flow, it merely changes the final deposited profile of the granular mass. The two distinct flowing masses eventually come to a rest at around  $t_s = 5.5$ . Evidently, this irregular type of evolution of the F/D interface makes it difficult to give a mathematical and practical description of the deposition rate within a depth-averaged context. For the case with  $a = 1.2$  and  $\theta = 10^\circ$ , and also for cases with  $\theta > 10^\circ$ , the initial potential energy and consequently the velocity of flow increases and the behavior of the F/D interface changes. More specifically, the interface divides the granular mass into deposited rear region and flowing frontal part that governs the runout. For such types of flow, the F/D interface moves toward the front of flow and the granular mass eventually comes to rest at times of  $t_s = 8.5$  and  $t_s = 13.5$  for  $\theta = 16^\circ$  and  $\theta = 22^\circ$ , respectively.

The inclined configuration of F/D interface (inset of Fig. 7-b) and the observed distinct flowing and deposited layers highlight the limitations of conventional DA models in simulating the physics of deposition. It can be inferred that the difference in the type of evolution of the F/D interface depends on both the initial aspect ratio  $a$  and slope angle. The separated parts of the granular mass (i.e., flow and deposited) for the case with  $a = 1.2$  and  $\theta = 10^\circ$ , and also for cases with  $\theta > 10^\circ$ , makes it possible to describe the evolution of the F/D interface mathematically and quantify the DA deposition rate in space and time (to be discussed).

Fig. 8 shows the temporal variations of the normalized total depth of granular mass  $h_T/H_0$  for the cases T16-A50, and T22-A70 at different locations along the slope.

At  $[x_M] = 0.0$ , the depth of granular mass initially equals to  $H_0$ . As the front of flow propagates down the slope, the total depth increases at first and then decreases to a relatively constant value when  $dh_T/dt \approx 0$ . For the case with  $a = 0.5$  and  $\theta = 16^\circ$ , the computed values of  $h_T/H_0$  at  $t_s > 6$  at different normalized positions along the slope range from 0.14 to 0.45. However, for the case with  $a = 0.7$  and  $\theta = 22^\circ$ , the values of  $h_T/H_0$  for  $t_s > 9$  range from 0.14 to 0.25. In the other words, by increasing the slope angle, the flow becomes thinner (i.e., shallow flow with  $h_T/x_\infty \ll 1$ ) and the variation in the total flow depth at distances along the slope is smaller (Fig. 7). Therefore, for flows over slope angles  $\theta > 10^\circ$ , the assumption that  $S_D = -dh_D/dt = dh/dt$  made in Section 2.2

appears to be a reasonable one.

The temporal variations in the normalized depth of deposited mass  $h_D/H_0$  at different locations along the slope for the cases T16-A50, T16-A120, T22-A70 and T22-A120 are shown in Fig. 9.

The trend lines have a correlation coefficient  $R^2 > 0.95$  and the slope of each line shows the normalized deposition rate  $(S_D)_s = [\sqrt{1/gH_0\cos\theta}] dh_D/dt$  at the corresponding location inside the granular mass. The data on the horizontal axis ( $h_D = 0$ ) shows the normalized critical time  $(t_s)_C$  at which the deposition starts and the F/D interface can be detected in the corresponding location. For instance, in  $[x_M] = 0.2$  deposition starts at  $(t_s)_C = 3.67$  and  $(t_s)_C = 6.89$  for the cases T16-A120 and T22-A120, respectively. After the normalized critical time, the F/D interface migrates towards the front of flow (Fig. 7) and deposition occurs at the downstream positions along the slope. Each normalized critical time corresponds to a critical value of the momentum of the flow in which the deposition process starts. In Section 4.2.2, the computed values of the critical momentum are obtained and used to quantify the deposition rate and close the depth-averaged Eqns. (10) and (11).

Different slopes of the trend lines show that the velocity of F/D interface in the flow-normal direction (i.e., deposition rate) is not constant along the flow length. It can be inferred that by increasing the slope angle, deposition occurs later compared to the cases with shallower slopes. Furthermore, deposition rate is inversely related to the slope angle, so by increasing the slope angle, the value of deposition rate decreases. This observed phenomena is consistent with the experimental results reported in the literature (Lube et al. 2011). Another point is that, for the same slope angle, by increasing  $a$ , the normalized critical time at the same normalized locations along the slope decreases and deposition occurs earlier compared to smaller values of  $a$ . With larger initial aspect ratios, the initial potential energy, and so the momentum along the flow-normal direction, increases (free-fall behavior (Lube et al. 2005)). Therefore, by increasing  $a$ , most of the motion duration occurs in flow-normal direction and deposition occurs at a smaller value of normalized time compared to cases with smaller initial aspect ratios.

The calculated normalized critical times for the onset of deposition at four different locations along the slope for the simulation cases in Table 1 are summarized in Table 3.

Fig. 10 shows the normalized velocity profiles ( $u_x/\sqrt{gH_0\cos\theta}$ ) in the normalized flow-normal direction ( $y/H_0$ ) for the cases T16-A50 and T22-A70.  $\sqrt{gH_0\cos\theta}$  is a characteristic velocity. The results are shown at locations of  $[x_M] = 0.2$  and  $0.4$  along the slope.

The non-zero values of the velocity at the base of flow are due to the slip velocity applied on the SPH particles close to the basal boundary (Nikooei and Manzari 2020). With increasing time, the velocity at the lower parts of the granular mass ( $y/H_0 < 0.1$ ) tend to decrease more compared to the higher parts due to the larger shear stress at the base of flow. At times larger than the critical value (i.e.,  $t_s > (t_s)_C$  in Table 3), the velocity at the lower parts of granular mass become smaller than the threshold value of 0.1 m/s (see Section 2.2) and deposition starts (the highlighted region). For instance, for case T22-A70 at location  $[x_M] = 0.2$  when  $t_s = 9$  (which is larger than  $(t_s)_C = 7.90$  mentioned in Table 3), the lower part of the velocity profile is in deposition region. In other words, the F/D interface has passed from  $[x_M] = 0.2$  at  $(t_s)_C = 7.90$  and the lower part of granular mass is in a deposition regime. During deposition, although the velocity of the granular mass at the lower parts reaches zero, the particles near the free surface move with a non-zero velocity (refer to the profiles at the last time steps in the shaded region).

#### 4.2.2. Critical depth-averaged momentum

In this section, a critical value for the momentum of the flow is found based on the calculated critical time for the onset of deposition. Moreover, the parameter  $a$  in the DA deposition model (Section 2.2) is quantified. The initial momentum of the flow depends on the geometry of the granular column. The inclination of the failure plane in a granular

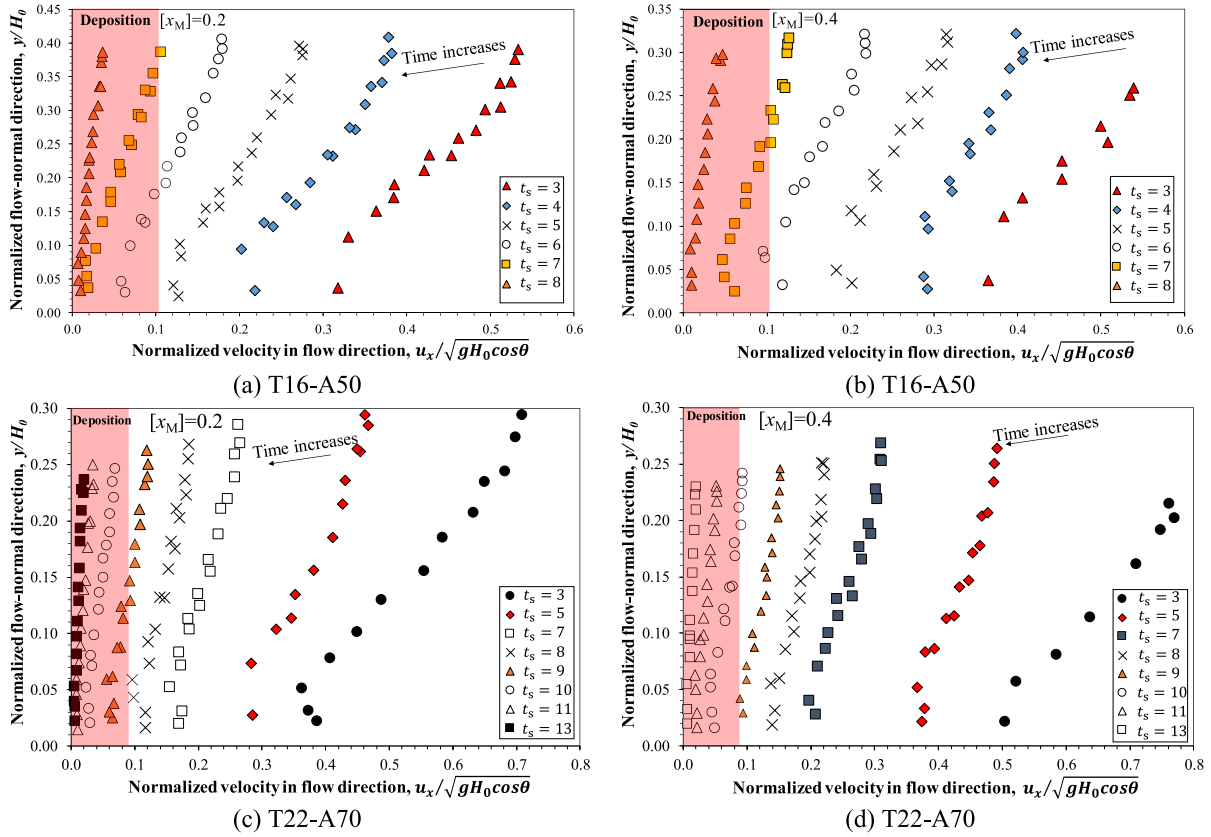


Fig. 10. Computed profile of normalized velocity in flow direction  $u_x / \sqrt{gH_0 \cos \theta}$  along the normalized flow-normal direction  $y/H_0$  during the time. The results are shown for cases a, b) T16-A50 and c, d) T22-A70 at two locations along the slope  $[x_M] = 0.2$  and  $[x_M] = 0.4$ .

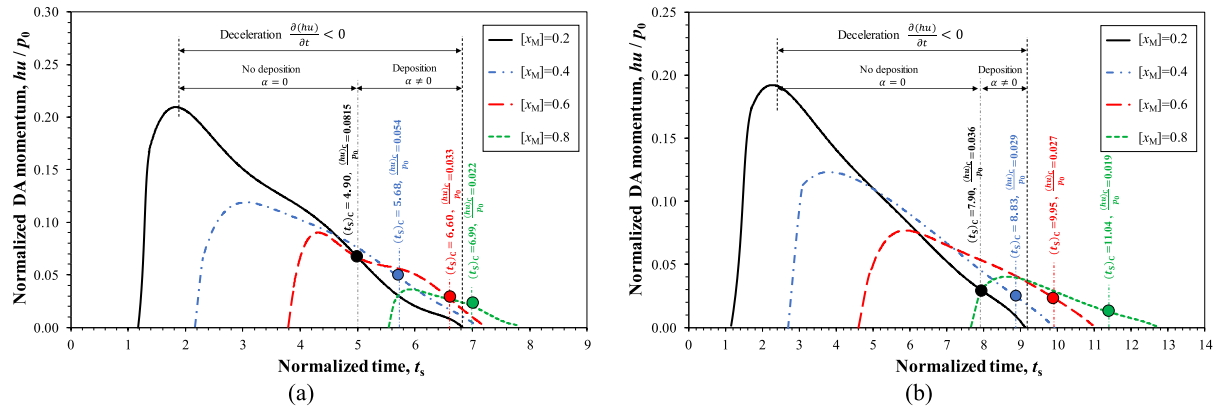


Fig. 11. Computed normalized DA momentum at different locations along the slope for cases a) T16-A50 and b) T22-A70. Different stages of deceleration process are also shown for  $[x_M] = 0.2$ . The circles show the normalized critical DA momentums at the corresponding normalized critical times.

mass can be obtained using Rankine’s theory, (i.e.,  $\theta_F = \pi/4 + \phi_1/2$ ) (Rankine 1857). For instance, for  $\phi_1 = 25.5^\circ$ , the inclination of the failure plane computed using 2D non-DA SPH simulations is  $55.8^\circ$  and is in good agreement with that calculated using Rankine’s theory  $\theta_F = 57.75^\circ$ . So, the initial amount of flowing mass and its associated momentum can be modeled properly.

The initial aspect ratio strongly influences the DA momentum and the onset of deposition. To generalize the results, the momentum of the flow is normalized by an approximate average of the initial momentum of the flow i.e.,  $p_0 = H_0 \sqrt{gH_0 \cos \theta}$ . In 2D,  $p_0$  is the product of  $M_0$  per density and initial length (i.e.  $H_0 = M_0/(\rho L_0)$ ) and the characteristic velocity.

Fig. 11 shows the temporal variations in the normalized DA momentum of the flow  $hu/p_0$  for the cases T16-A50 and T22-A70 at different locations along the slope.

Different stages of the deceleration process are shown for  $[x_M] = 0.2$ . For instance, for the case T22-A70 at around  $t_s = 1.2$ , the front of flow reaches the location  $[x_M] = 0.2$  and the normalized DA momentum increases. After that, the flow decelerates due to the internal and basal friction forces (i.e.,  $d(hu)/dt < 0$ ). When the normalized DA momentum becomes smaller than a normalized critical DA momentum  $(hu)_c/p_0$  at the corresponding normalized critical time  $(t_s)_c$  (the circle symbols), the F/D interface reaches the monitoring section at the location  $[x_M] = 0.2$  and the onset of deposition occurs (Fig. 9). After finding  $(t_s)_c$ , as

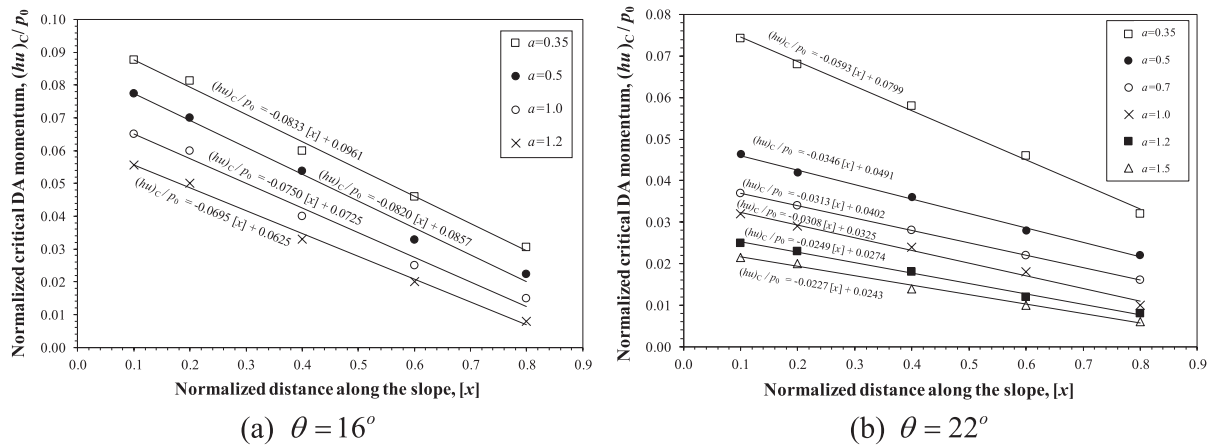


Fig. 12. Computed values of the normalized critical DA momentum versus the normalized distance along the slope for different values of initial aspect ratio. The results are shown for the cases with a)  $\theta = 16^\circ$  and b)  $\theta = 22^\circ$ .

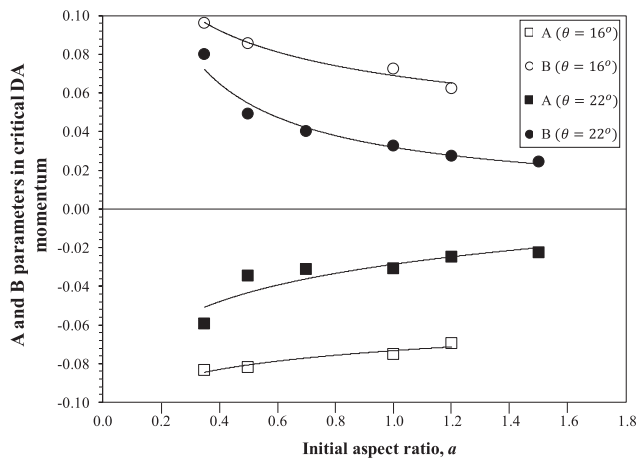


Fig. 13. The parameters of A and B for the critical DA momentum equation calculated for different initial aspect ratios and slope angles.

Table 4

Effects of normalized location along the slope, initial aspect ratio and slope angle on the normalized deposition parameters (critical time, critical DA momentum and deposition rate).

Parameter change	Critical time	Critical DA momentum	Deposition rate
Increase in $[x]$	Increase	Decrease	–
Increase in $\theta$	Increase	Decrease	Decrease
Increase in $a$	Decrease	Decrease	–

explained in Section 4.2.1, the value of  $(hu)_C/p_0$  can be calculated (Fig. 11) at different locations along the slope.

For values of  $hu > (hu)_C$ , the momentum of flow is large and deposition does not occur. Therefore, by setting a zero value for the coefficient  $\alpha$  in Eq. (14), the deposition rate will be computed as zero. However, for values of  $hu < (hu)_C$ , the momentum of the flow is small and the internal and basal resistance forces induce deposition. So, the coefficient  $\alpha$  can be defined as a function that depends on the DA momentum, which plays a crucial role in the deposition process at different locations along the path. For simplicity, a linear relation for  $\alpha$  as a function of  $hu$  is assumed as follows:

$$\alpha = \begin{cases} 0 & \text{if } hu > (hu)_C \\ \frac{(hu)_C - hu}{(hu)_C} & \text{if } hu < (hu)_C \text{ \& } \frac{d(hu)}{dt} < 0 \end{cases} \quad (34)$$

This equation returns a value of  $\alpha$  for the calculation of the deposition rate in Eq. (14). The critical DA momentum depends on different parameters, including the initial momentum of the flow, the internal and basal frictions, the slope angle, and the distance traveled by the flow. In this study we incorporate the effects of deposition into the depth-averaged context and the influences of two controlling parameters  $a$  and  $\theta$  on the deposition process are evaluated. The normalized form of relation between  $(hu)_C/p_0$  and the variables  $a$  and  $\theta$  at each normalized location along the slope  $[x] = (x - L_0)/(x_\infty - L_0)$  can be written as follows:

$$\frac{(hu)_C}{p_0} = F(a, \theta, [x]). \quad (35)$$

Fig. 12 shows the calculated values of  $(hu)_C/p_0$  versus  $[x]$  for the cases with  $\theta = 16^\circ$  and  $\theta = 22^\circ$ . The results are shown for different initial aspect ratios. Each trend line is shown and has approximately a correlation coefficient of  $R^2 = 0.99$ . Fig. 13 shows the calculated values of parameters A and B from Fig. 12 for different initial aspect ratios for slope angles of  $16^\circ$  and  $22^\circ$ .

From the results of the 2D non-DA SPH model, the generalized relation for the normalized critical DA momentum can be given as follows:

$$\frac{(hu)_C}{p_0} = A[x] + B. \quad (36)$$

where  $A < 0$  and  $B > 0$  and these parameters depend on  $a$  and  $\theta$ . This generalized relation for critical DA momentum is applicable for cases under simplifying assumptions made in this paper (i.e., dense and dry granular flows, and flow over rigid beds with steep slopes).

For each value of the initial aspect ratio, the normalized critical DA momentum decreases linearly with downslope position. Therefore, it can be inferred that deposition occurs at smaller values of DA momentum at more distal locations from the initial granular mass. This result is due to this fact that, although the velocity of flow is larger at distal locations, smaller depth of flow at these locations leads to a smaller value of DA momentum compared to the proximal locations (Fig. 11). By increasing of  $a$  and  $\theta$  (increasing the initial velocity), the values of A and B and equivalently the value of  $(hu)_C/p_0$  decrease. When the initial velocity of flow increases, the flow has larger value of initial momentum and consequently, the values of  $(hu)_C/p_0$  and B (the intercept of linear function of  $(hu)_C/p_0$ ) decrease compared to the smaller

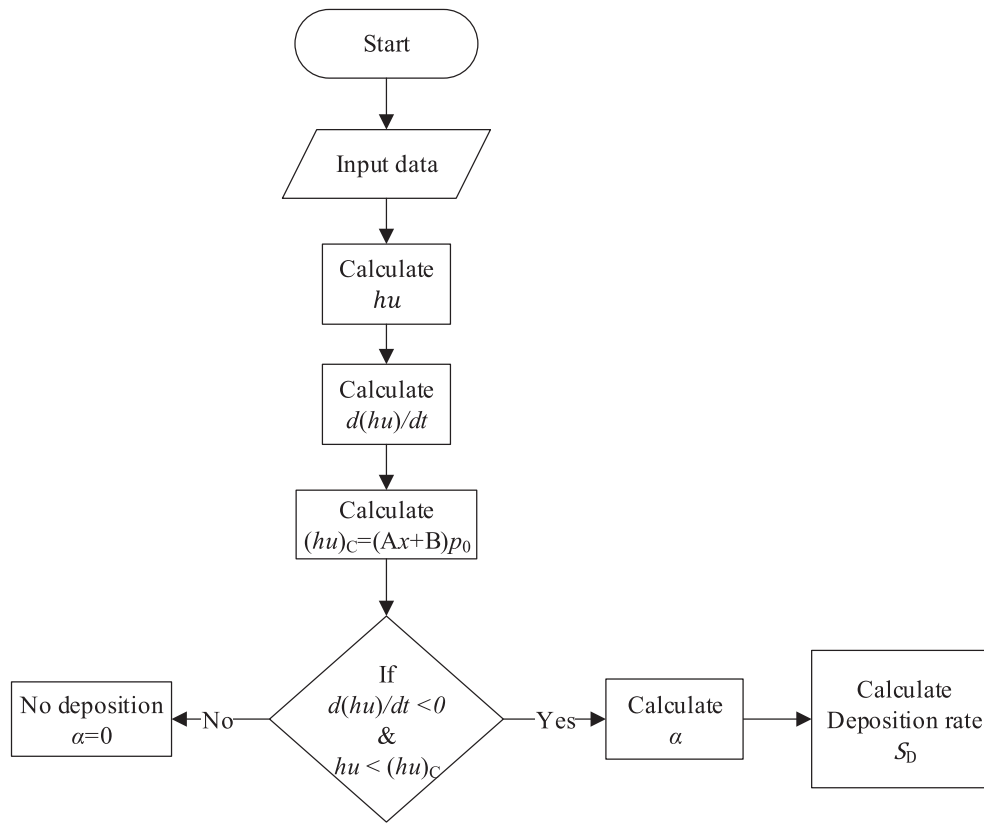


Fig. 14. Algorithm for calculation of the deposition rate as a source term in the main DA SPH code.

Table 5

Simulation cases for studying the effects of deposition on runoff of 1D flow ( $\theta = 22^\circ$ ). The internal and basal friction angles are  $\phi_1 = \phi_B = 25.5^\circ$ .

Case ID	$a$	$L_0$ (m)	$H_0$ (m)	A	B
1D-A30	0.3	0.300	0.090	-0.0541	0.0814
1D-A45	0.45	0.250	0.113	-0.0455	0.0594
1D-A70	0.7	0.200	0.140	-0.0313	0.0402
1D-A124	1.24	0.150	0.186	-0.0240	0.0270

values of  $a$  and  $\theta$ . In addition, as the velocity of flow increases, the flow becomes shallower and variations in the depth of flow along the slope decrease (compare Fig. 7-d and Fig. 7-e). Therefore, since the DA momentum depends on the flow depth, by increasing of  $a$  and  $\theta$ , the dependency of DA momentum on the distance along the slope (the coefficient A) decreases. Consequently, in practical DA models for hazard assessment, the assumption of a constant value for A for cases with large values of initial aspect ratio and slope angle appear to be a reasonable one.

Finally, the effects of the variations in parameters  $[x]$ ,  $a$  and  $\theta$  on the normalized deposition parameters (critical time, critical DA momentum and deposition rate) are summarized in Table 4. A systematic relationship between the effects of  $[x]$  and  $a$  on the deposition rate is not found.

The main output of the 2D non-DA SPH model is the generalized relationship for the critical DA momentum and  $a$  at different location of a flow. Fig. 14 shows the algorithm for calculating of the deposition rate  $S_D$  based on the generalized relationships, which will be added to the main algorithm of DA SPH model (Fig. 4).

To calculate the DA deposition rate, the parameters A and B need to be determined based on the initial aspect ratio and slope of the simulation (Fig. 13). After that, the critical DA momentum at the onset of deposition at different locations is calculated using generalized Eq. (36) at each time step. By comparing the value of DA momentum for each

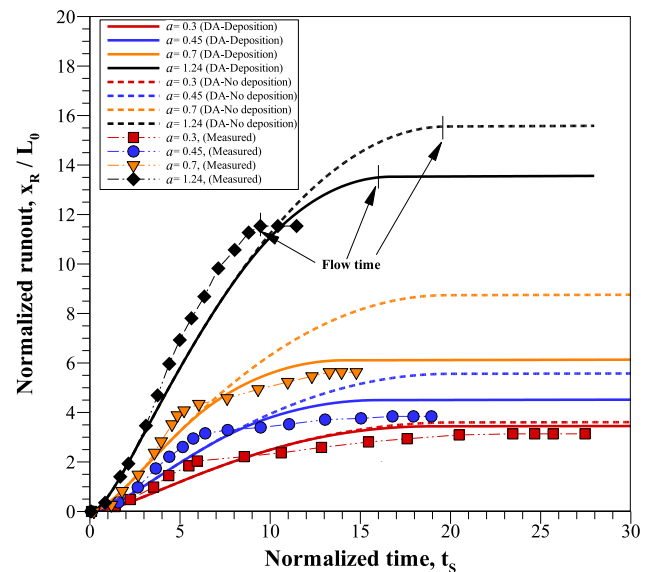


Fig. 15. Comparison of the normalized runoff for different values of initial aspect ratio among the computed (DA SPH models with and without deposition) results and measured data (Farin et al. 2014). Normalized flow time  $t_F$  is shown for  $a = 1.24$ .

SPH particle with the critical DA momentum at the corresponding location, the parameter  $\alpha$  is calculated using Eq. (34). Finally, the deposition rate (Eq. (14)) will close the depth-averaged form of Eqns. (10) and (11).

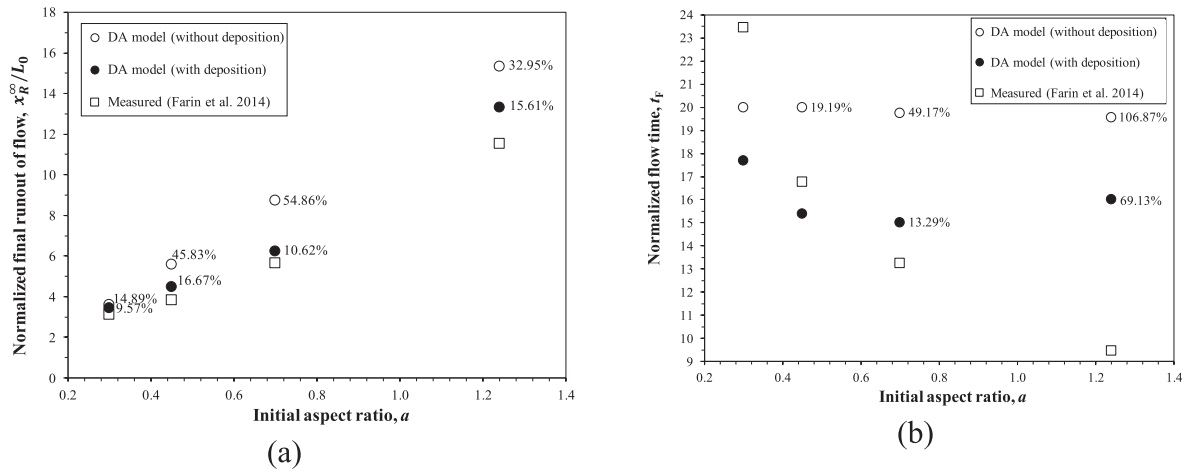


Fig. 16. Comparison of the a) normalized final runoff and b) normalized flow time among the computed (DA SPH models with and without deposition) results and measured data (Farin et al. 2014). The relative error ((computed-measured)/measured  $\times$  100%) is shown for both the DA models.

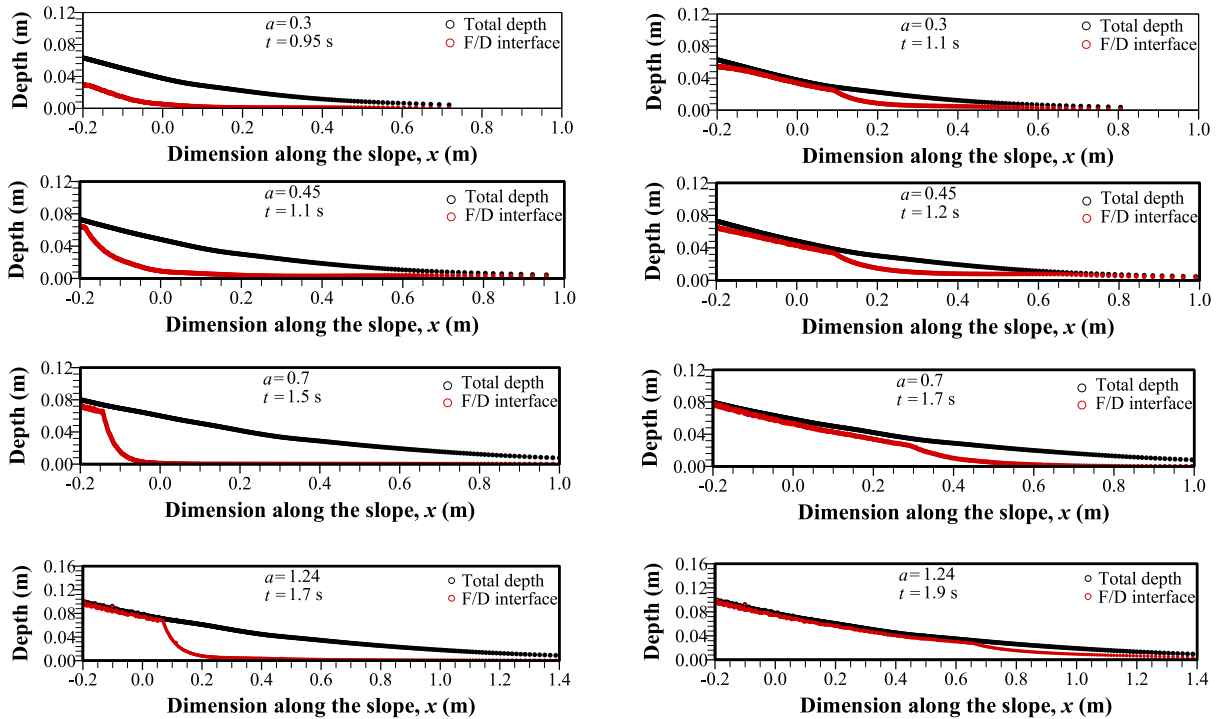


Fig. 17. Computed profiles of total depth  $h_T$  and deposited mass  $h_D$  (F/D interface) for different simulation cases using 1D SPH model. The results for each case are shown for two different times ( $\theta = 22^\circ$ ).

### 4.3. Evaluation of DA simulation results

(Farin et al. 2014) conducted experiments on the collapse of columns with different initial aspect ratios of 0.3, 0.45, 0.7, and 1.24 over an inclined plane with a slope angle of  $22^\circ$ . Here, these cases are simulated using the DA models with and without considering the effects of deposition. To model the effects of deposition using the new DA model, parameters A and B need to be firstly defined. For instance, for an initial aspect ratio of 0.3, the initial depth and momentum are  $H_0 = 0.09$  m and  $p_0 = 0.0814$   $m^2/s$ , respectively. The coefficients are  $A = -0.0541$  and  $B = 0.0814$  (Fig. 13). The values of coefficients A and B obtained from the results of 2D non-DA SPH model (Fig. 12) are shown in this Table 5. The internal and basal friction angles are  $\phi_I = \phi_B = 25.5^\circ$ .

Fig. 15 shows a comparison of the computed normalized runoff of

flow using the DA SPH model and measured data reported by (Farin et al. 2014). The numerical results are shown for the DA models with and without considering the effects of deposition. The runoff of the flow in the one-dimensional DA model (Fig. 3) is normalized by the initial length i.e.,  $x_R/L_0$ . The vertical lines on the curves for  $a = 1.24$  show the normalized flow time  $t_f$  of the flow (i.e., the time when the flow comes to rest).

Fig. 16 shows the computed and measured data for the normalized final runoff  $x_R^\infty/L_0$  and normalized flow time. The error percentage relative to the measured data ((computed-measured)/measured  $\times$  100%) is shown for both the DA models with and without the effects of deposition.

The results show that the DA model without deposition predicts the final runoff and flow time with maximum errors of 55% for  $a = 0.7$  and 107% for  $a = 1.24$ , respectively. This discrepancy could be due to fact

that the DA model without the effects of deposition do not explicitly consider the stopping of the flow due to the evolution of the F/D interface.

By incorporating the deposition model, the final runout and flow time are reconstructed and predicted with maximum errors of 17% for  $a = 0.45$  and 69% for  $a = 1.24$ , respectively. Therefore, the DA model with the effects of deposition improves the estimation of runout and flow time by 38% compared to the DA model without the effects of deposition. For cases with  $a = 0.3$  and  $a = 0.45$ , the DA model underestimates the flow time, which is due to the disability of this model to capture the slow propagation phase that extends the duration of flow (Farin et al. 2014). However, the new DA model can predict the final value of runout with a reasonable accuracy.

Overestimation of the runout by DA model mainly occurs during the final stages of the flow (deceleration regime), which shows the importance of modelling the effects of the deposition during deceleration. From the comparison of the results of the DA models with and without the effects of deposition, it can be inferred that by considering the effects of deposition, the runout of the flow does not change in the acceleration phase (initial stage) and will be reproduced during deceleration stage. Although the improvements made in numerical simulation by the deposition effects, there remain challenges that need to be addressed:

- The overestimation of the results by DA models with and without the consideration of the effects of deposition is caused by simplifications made during the initial motion of the granular mass in the flow-normal direction (i.e., free-fall phase) and partial failure of granular mass that affects the momentum of the flow and the subsequent deposition process (Fig. 7). Therefore, capturing the realistic physics during the initial failure and motion of granular mass can improve predictions.
- The initial aspect ratio and the slope angle are considered as the two main controlling parameters on the critical DA momentum of flow and deposition. However, the internal friction angle also governs the deposition rate and the momentum change of the flow as was shown in Fig. 1. We adopt a constant value for internal and basal friction angles, which are simplifications of what happens in reality. Studying the effects of variations of these parameters on the results remains an open question for further research.

In this study, for the first time, the effects of the evolution of the F/D interface is incorporated into the deposition process of a granular flow in depth-averaged context. Fig. 17 shows the total depth and F/D interface for cases in Table 5 at two different times.

As the collapse progresses, the F/D interface moves towards the front of flow before the granular material comes to rest. When the F/D interface intersects the free surface of the flow, the granular mass beneath it deposits and comes to rest. The effective depth of flowing mass at each location is a critical input for the DA governing Eqns. (10) and (11). In DA models without considering the effects of deposition, the total depth is used to compute the momentum of the flow. Since the total depth is larger than the effective depth of flow ( $h_T > h$ ), DA models that do not consider the effects of deposition tend to overestimates the momentum. In the DA model that considers the effects of deposition, the effective depth of flow is smaller than the total depth and the upper portion of the total mass contributes into the governing equations. This effective depth of flow plays an important role in the decay of the flow momentum to reduce the runout (Fig. 15).

## 5. Conclusions

A novel framework to model the deposition of granular flows using a depth-averaged approach is proposed. A new deposition model that considers the initial aspect ratio and slope angle was developed based on a high-fidelity 2D non-DA SPH solver. The deposition model is then implemented in a DA model and evaluated using experimental results published in the literature. Conclusions of this study can be drawn as follows:

- 1) For the first time, the effects of the evolution of F/D interface is introduced into the deposition process of a one-dimensional granular flow in depth-averaged context using a high-fidelity 2D non-DA SPH method. This can be regarded as a new paradigm of development for the future incorporation of deposition and erosion in the depth-averaged context. By capturing the internal dynamics of granular mass using higher order numerical models, physical-based deposition/erosion models can be adopted instead of the purely empirical ones in DA framework. The physical-based models can reveal the evolution of internal F/D interface and improve the realistic prediction of runout and deposited volume of flow.
- 2) Existing depth-averaged models overestimate the runout and flow time. It is shown that by considering the effects of deposition, the DA model improves the estimation of the runout and flow time by up to 38%, compared to the DA model without deposition. Although the newly-developed DA model improves the runout and flow time prediction, the details of the collapse process, such as the initial flow-normal motion and the incomplete failure of granular mass based on Rankine's theory are overlooked. Incorporation of these details as well as the effects of deposition into the conventional DA models can improve their applicability for hazard assessment of flow type landslides.
- 3) Deposition is responsible for decaying the flow momentum from the critical DA momentum. This critical value determines the threshold for the onset of deposition at each location of the granular mass. The critical DA momentum is found to be a linear function of the flow length and its parameters are assumed to depend on the initial aspect ratio and slope angle. The relationship may be leveraged for the future development of more sophisticated relationships for modelling the effects of erosion and deposition in the DA framework.

## CRedit authorship contribution statement

**Mohammad Nikooei:** Software, Writing- original draft, Writing – review & editing, Formal analysis, Methodology, Validation, Data curation. **Clarence Edward Choi:** Supervision, Funding acquisition, Methodology, Writing – review & editing, Validation

## Declaration of Competing Interest

The authors declare that they have no known competing financial interests or personal relationships that could have appeared to influence the work reported in this paper.

## Acknowledgements

The authors are grateful for the generous financial sponsorship from the Research Grants Council of Hong Kong (General Research Fund Grants 16209717; 16210219; 27205320; AoE/E-603/18).

Appendix

To study the effects of the width of monitoring section on the results of 2D non-DA SPH model (see Section 3), four different values of  $W_M = \Delta x, 2\Delta x, 3\Delta x, 4\Delta x$  are considered and the normalized values of DA momentum at different locations along the slope are shown in Fig. A.1. The initial particle spacing in the 2D non-DA SPH model is  $\Delta x = 0.004\text{ m}$ . For the case with  $W_M = \Delta x$ , the DA momentum cannot be computed accurately because the monitoring section is too narrow and no meaningful average can be obtained. The results are shown for the case with  $a = 0.7$  and  $\theta = 22^\circ$  and during deceleration stage (i.e.,  $d(hu)/dt < 0$ ).

The root mean square (RMS) of deviation of the computed results for cases with  $W_M = 3\Delta x$  and  $4\Delta x$  relative to the case with  $W_M = 2\Delta x$  (i.e.,  $\text{RMS} = \sqrt{\frac{1}{n} \sum_{k=0}^n ([hu/p_0]_k - [hu/p_0]_{W_M=2\Delta x})^2}$ ) is calculated and shown in Fig. A.2. Where  $n$  refers to the number of data points at each case. The results are shown for  $\theta = 22^\circ$ .

The results show that the deviation of the results for  $W_M = 4\Delta x$  is larger than  $W_M = 3\Delta x$ . However, the RMS values smaller than 0.03 show that increasing the width of monitoring section larger than  $2\Delta x$  does not have significant effects on of the averaging of  $h$  and  $u$  for SPH particles at each location. As it is shown in Fig. A.1, the DA momentum does not change by increasing  $W_M$  especially at final times for each location. It should be noted that by decreasing the time step, the DA momentum of particles for cases with  $W_M = \Delta x$  can be captured, however, the computational cost increases. Therefore, to obtain a reasonable resolution and to reduce the computational cost,  $W_M = 2\Delta x$  is selected for rest of calculations as was discussed in Section 4.2.1.

Fig. A.3 shows the evolution of the F/D interface for cases listed in Table 1.

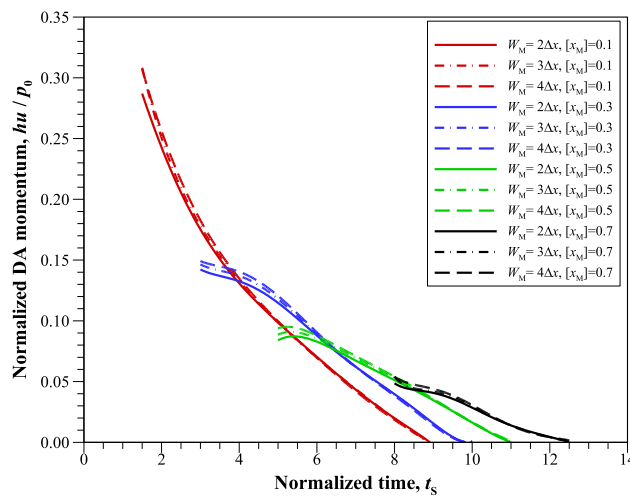


Fig. A1. Computed temporal variations in normalized DA momentum at different locations along the slope for case with  $a = 0.7$  and  $\theta = 22^\circ$ . Different values of width of monitoring section are considered to study its effects on the results.

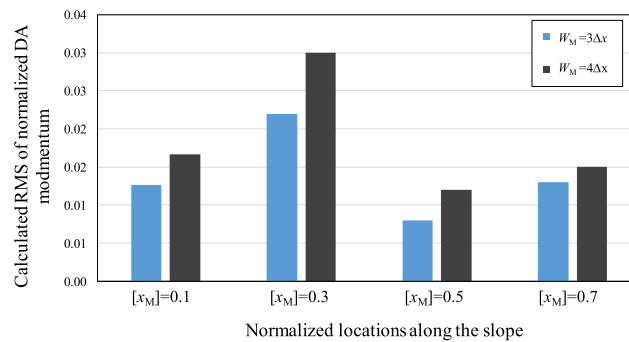


Fig. A2. Calculated RMS of deviation of normalized DA momentum relative to the case with  $W_M = 2\Delta x$  at different locations along the slope ( $\theta = 22^\circ$ ). Different values of width of monitoring section are considered to study its effects on the results.

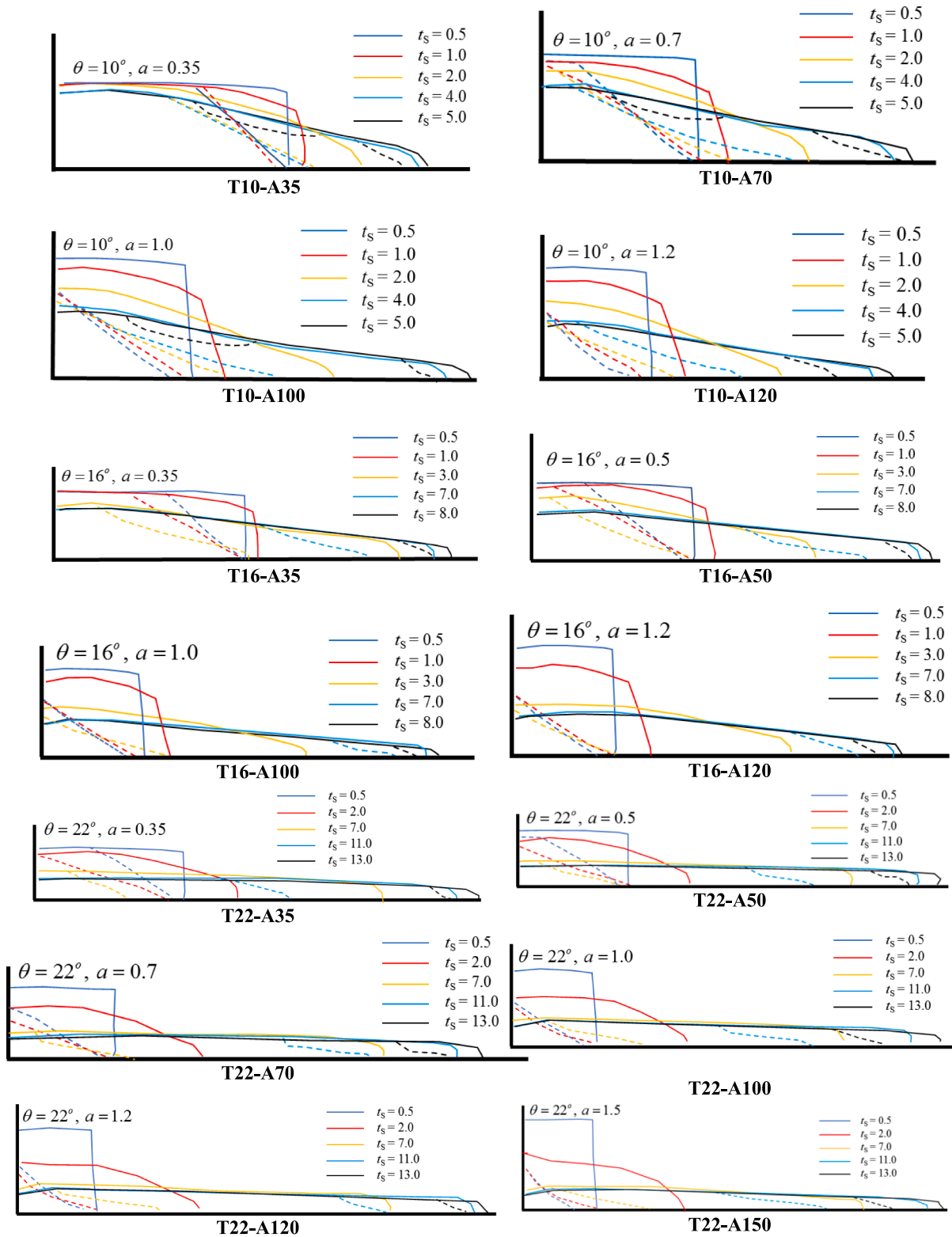


Fig. A3. Temporal evolution of the profiles of the F/D interface (dashed line) for different cases. The results are shown at normalized time  $t_s$ .

## References

- Artoni, R., Santomaso, A., 2014. Effective wall slip in chutes and channels: experiments and discrete element simulations. *Granular Matter* 16 (3), 377–382.
- Baselt, L., de Oliveira, G.Q., Fischer, J.-T., Pudasaini, S.P., 2021. Deposition morphology in large-scale laboratory stony debris flows. *Geomorphology* 107992.
- Bui, H.H., Nguyen, G.D., 2021. Smoothed particle hydrodynamics (SPH) and its applications in geomechanics: From solid fracture to granular behaviour and multiphase flows in porous media. *Comput. Geotech.* 138, 104315.
- Calvello, M., Cuomo, S., Ghasemi, P., 2017. The role of observations in the inverse analysis of landslide propagation. *Comput. Geotech.* 92, 11–21.
- Choi, C.E., Cui, Y., Au, K.Y.K., Liu, H., Wang, J., Liu, D., Wang, H., 2018. Case study: effects of a partial-debris dam on riverbank erosion in the Parlung Tsangpo River, China. *Water* 10 (3), 250.
- Choi, C.E., Goodwin, G.R., 2021. Effects of interactions between transient granular flows and macroscopically rough beds and their implications for bulk flow dynamics. *Can. Geotech. J.* 99 (999), 1943–1960.
- Colagrossi, A. (2005). "A meshless Lagrangian method for free-surface and interface flows with fragmentation." [These, Universita di Roma.](#)
- Cremonesi, M., Ferri, F., Perego, U., 2017. A basal slip model for Lagrangian finite element simulations of 3D landslides. *Int. J. Numer. Anal. Meth. Geomech.* 41 (1), 30–53.
- Crosta, G., De Blasio, F., De Caro, M., Volpi, G., Imposimato, S., Roddeman, D., 2017. Modes of propagation and deposition of granular flows onto an erodible substrate: experimental, analytical, and numerical study. *Landslides* 14 (1), 47–68.
- Crosta, G., Imposimato, S., Roddeman, D., 2009. Numerical modeling of 2-D granular step collapse on erodible and nonerodible surface. *J. Geophys. Res. Earth Surf.* 114 (F3).
- Cui, X., Gray, J., 2013. Gravity-driven granular free-surface flow around a circular cylinder. *J. Fluid Mech.* 720, 314–337.
- Cui, X., Gray, J.N.T., Johannesson, T., 2007. Deflecting dams and the formation of oblique shocks in snow avalanches at Flateyri, Iceland. *J. Geophys. Res. Earth Surf.* 112 (F4).
- De Haas, T., Braat, L., Leuven, J.R., Lokhorst, I.R., Kleinhans, M.G., 2015. Effects of debris flow composition on runout, depositional mechanisms, and deposit morphology in laboratory experiments. *J. Geophys. Res. Earth Surf.* 120 (9), 1949–1972.
- Doyle, E.E., Huppert, H.E., Lube, G., Mader, H.M., Sparks, R.S.J., 2007. Static and flowing regions in granular collapses down channels: insights from a sedimenting shallow water model. *Phys. Fluids* 19 (10), 106601.
- Drucker, D.C., Prager, W., 1952. Soil mechanics and plastic analysis or limit design. *Q. Appl. Math.* 10 (2), 157–165.
- Dufresne, A., 2012. Granular flow experiments on the interaction with stationary runout path materials and comparison to rock avalanche events. *Earth Surf. Proc. Land.* 37 (14), 1527–1541.
- Edwards, A., Gray, J., 2015. Erosion–deposition waves in shallow granular free-surface flows. *J. Fluid Mech.* 762, 35–67.
- Edwards, A., Viroulet, S., Johnson, C., Gray, J., 2021. Erosion-deposition dynamics and long distance propagation of granular avalanches. *J. Fluid Mech.* 915.
- Edwards, A., Viroulet, S., Kokelaar, B., Gray, J., 2017. Formation of levees, troughs and elevated channels by avalanches on erodible slopes. *J. Fluid Mech.* 823, 278–315.
- Farin, M., Mangeney, A., Roche, O., 2014. Fundamental changes of granular flow dynamics, deposition, and erosion processes at high slope angles: insights from laboratory experiments. *J. Geophys. Res. Earth Surf.* 119 (3), 504–532.
- Fatehi, R., Manzari, M.T., 2012. A consistent and fast weakly compressible smoothed particle hydrodynamics with a new wall boundary condition. *Int. J. Numer. Meth. Fluids* 68 (7), 905–921.
- Fernández-Nieto, E.D., Garres-Díaz, J., Mangeney, A., Narbona-Reina, G., 2018. 2D granular flows with the  $\mu$  (I) rheology and side walls friction: a well-balanced multilayer discretization. *J. Comput. Phys.* 356, 192–219.
- Forterre, Y., Pouliquen, O., 2008. Flows of dense granular media. *Annu. Rev. Fluid Mech.* 40, 1–24.
- Ghilardi, P., Natale, L., Savi, F., 2001. Modeling debris flow propagation and deposition. *Phys. Chem. Earth Part C* 26 (9), 651–656.
- Gingold, R.A., Monaghan, J.J., 1977. Smoothed particle hydrodynamics: theory and application to non-spherical stars. *MNRAS* 181 (3), 375–389.
- Goodwin, G.R., Choi, C.E., 2022. A depth-averaged SPH study on spreading mechanisms of geophysical flows in debris basins: Implications for terminal barrier design requirements. *Comput. Geotech.* 141, 104503.
- Gray, J., Edwards, A., 2014. A depth-averaged-rheology for shallow granular free-surface flows. *J. Fluid Mech.* 755, 503–534.
- Gray, J.M.N.T., Wieland, M., Hutter, K., 1999. Gravity-driven free surface flow of granular avalanches over complex basal topography. *Proc. R. Soc. Lond. A* 455 (1985), 1841–1874.
- He, X., Liang, D., Bolton, M., 2018. Run-out of cut-slope landslides: mesh-free simulations. *Géotechnique* 68 (1), 50–63.
- Hongbin, J., Xin, D., 2005. On criteria for smoothed particle hydrodynamics kernels in stable field. *J. Comput. Phys.* 202 (2), 699–709.
- Hosseini, S. M., M. T. Manzari and S. k. Hannani (2007). "A fully explicit three-step SPH algorithm for simulation of non-Newtonian fluid flow." *Int. J. Numer. Methods Heat Fluid Flow* 17(7): 715–735.
- Hungr, O., 1995. A model for the runout analysis of rapid flow slides, debris flows, and avalanches. *Can. Geotech. J.* 32 (4), 610–623.
- Hungr, O., Leroueil, S., Picarelli, L., 2014. The Varnes classification of landslide types, an update. *Landslides* 11 (2), 167–194.
- Hutter, K., Siegel, M., Savage, S., Nohguchi, Y., 1993. Two-dimensional spreading of a granular avalanche down an inclined plane Part I. theory. *Acta Mech.* 100 (1), 37–68.
- Ionescu, I.R., 2013. Augmented Lagrangian for shallow viscoplastic flow with topography. *J. Comput. Phys.* 242, 544–560.
- Ionescu, I.R., Mangeney, A., Bouchut, F., Roche, O., 2015. Viscoplastic modeling of granular column collapse with pressure-dependent rheology. *J. Nonnewton. Fluid Mech.* 219, 1–18.
- Iverson, R.M., 1997. The physics of debris flows. *Rev. Geophys.* 35 (3), 245–296.
- Iverson, R.M., 2012. Elementary theory of bed-sediment entrainment by debris flows and avalanches. *J. Geophys. Res. Earth Surf.* 117 (F3).
- Jop, P., Forterre, Y., Pouliquen, O., 2006. A constitutive law for dense granular flows. *Nature* 441 (7094), 727–730.
- Koo, R.C., Kwan, J.S., Lam, C., Goodwin, G.R., Choi, C., Ng, C., Yiu, J., Ho, K., Pun, W., 2018. Back-analysis of geophysical flows using three-dimensional runout model. *Can. Geotech. J.* 55 (8), 1081–1094.
- Lajeunesse, E., Monnier, J., Homsy, G., 2005. Granular slumping on a horizontal surface. *Phys. Fluids* 17 (10), 103302.
- Larrieu, E., Staron, L., Hinch, E., 2006. Raining into shallow water as a description of the collapse of a column of grains. *J. Fluid Mech.* 554, 259–270.
- Lee, E.-S., Moulinec, C., Xu, R., Violeau, D., Laurence, D., Stansby, P., 2008. Comparisons of weakly compressible and truly incompressible algorithms for the SPH mesh free particle method. *J. Comput. Phys.* 227 (18), 8417–8436.
- Lube, G., Cronin, S.J., Platz, T., Freundt, A., Procter, J.N., Henderson, C., Sheridan, M.F., 2007. Flow and deposition of pyroclastic granular flows: A type example from the 1975 Ngauruhoe eruption. *New Zealand J. Volcanol. Geoth. Res.* 161 (3), 165–186.
- Lube, G., Huppert, H.E., Sparks, R.S.J., Freundt, A., 2005. Collapses of two-dimensional granular columns. *Phys. Rev. E* 72 (4), 041301.
- Lube, G., Huppert, H.E., Sparks, R.S.J., Freundt, A., 2007. Static and flowing regions in granular collapses down channels. *Phys. Fluids* 19 (4), 043301.
- Lube, G., Huppert, H.E., Sparks, R.S.J., Freundt, A., 2011. Granular column collapses down rough, inclined channels. *J. Fluid Mech.* 675, 347.
- Mamouni, S.J., Fatehi, R., Manzari, M.T., 2015. A consistent incompressible SPH method for internal flows with fixed and moving boundaries. *Int. J. Numer. Meth. Fluids* 81 (10), 589–610.
- Mangeney, A., Bouchut, F., Vilotte, J., Lajeunesse, E., Aubertin, A., Pirulli, M., 2005. On the use of Saint Venant equations to simulate the spreading of a granular mass. *J. Geophys. Res. Solid Earth* 110 (B9).
- Mangeney, A., Roche, O., Hungr, O., Mangold, N., Faccanoni, G., Lucas, A., 2010. Erosion and mobility in granular collapse over sloping beds. *J. Geophys. Res. Earth Surf.* 115 (F3).
- Mangeney, A., Tsimring, L., Volfson, D., Aranson, I.S., Bouchut, F., 2007. Avalanche mobility induced by the presence of an erodible bed and associated entrainment. *Geophys. Res. Lett.* 34 (22).
- McDougall, S., 2006. A new continuum dynamic model for the analysis of extremely rapid landslide motion across complex, 3D terrain. University of British Columbia.
- McDougall, S., Hungr, O., 2004. A model for the analysis of rapid landslide motion across three-dimensional terrain. *Can. Geotech. J.* 41 (6), 1084–1097.
- McDougall, S., Hungr, O., 2005. Dynamic modelling of entrainment in rapid landslides. *Can. Geotech. J.* 42 (5), 1437–1448.
- Medina, V., Hürlimann, M., Bateman, A., 2008. Application of FLATModel, a 2D finite volume code, to debris flows in the northeastern part of the Iberian Peninsula. *Landslides* 5 (1), 127–142.
- Monaghan, J., 1985. Particle methods for hydrodynamics. *Comput. Phys. Rep.* 3 (2), 71–124.
- Monaghan, J.J., 1992. Smoothed particle hydrodynamics. *Ann. Rev. Astron. Astrophys.* 30 (1), 543–574.
- Monaghan, J.J., 2000. SPH without a tensile instability. *J. Comput. Phys.* 159 (2), 290–311.
- Morris, J., 1996. Analysis of SPH with applications. Monash University, Melbourne, Australia.
- Ng, C.W.W., Choi, C., Law, R.P., 2013. Longitudinal spreading of granular flow in trapezoidal channels. *Geomorphology* 194, 84–93.
- Ng, C.W.W., Choi, C.E., Goodwin, G.R., 2019. Froude characterization for unsteady single-surge dry granular flows: impact pressure and runup height. *Can. Geotech. J.* 56 (12), 1968–1978.
- Nikooei, M., Manzari, M.T., 2020. Studying effect of entrainment on dynamics of debris flows using numerical simulation. *Comput. Geosci.* 134, 104337.
- Nikooei, M., Manzari, M.T., 2021. Investigating the effect of mixing layer rheology on granular flow over entrainable beds using SPH method. *Comput. Geosci.* 155, 104792.
- Pastor, M., Blanc, T., Haddad, B., Petrone, S., Sanchez Morles, M., Drempetic, V., Issler, D., Crosta, G.B., Cascini, L., Sorbino, G., Cuomo, S., 2014. Application of a SPH depth-integrated model to landslide run-out analysis. *Landslides* 11 (5), 793–812.
- Peng, C., Li, S., Wu, W., An, H., Chen, X., Ouyang, C., Tang, H., 2022. On three-dimensional SPH modelling of large-scale landslides. *Can. Geotech. J.* 59 (1), 24–39.
- Peng, C., Wang, S., Wu, W., Yu, H.-S., Wang, C., Chen, J.-Y., 2019. LOQUAT: an open-source GPU-accelerated SPH solver for geotechnical modeling. *Acta Geotech.* 14 (5), 1269–1287.
- Pudasaini, S.P., Fischer, J.-T., 2020. A mechanical erosion model for two-phase mass flows. *Int. J. Multiph. Flow* 132, 103416.
- Randles, P., Libersky, L.D., 1996. Smoothed particle hydrodynamics: some recent improvements and applications. *Comput. Methods Appl. Mech. Eng.* 139 (1–4), 375–408.

- Rankine, W. J. M. (1857). "II. On the stability of loose earth." Philosophical transactions of the Royal Society of London(147): 9-27.
- Rauter, M., Barker, T., Fellin, W., 2020. Granular viscosity from plastic yield surfaces: the role of the deformation type in granular flows. *Comput. Geotech.* 122, 103492.
- Rauter, M., Köhler, A., 2020. Constraints on entrainment and deposition models in avalanche simulations from high-resolution radar data. *Geosciences* 10 (1), 9.
- Sarno, L., Carravetta, A., Martino, R., Tai, Y., 2014. A two-layer depth-averaged approach to describe the regime stratification in collapses of dry granular columns. *Phys. Fluids* 26 (10), 103303.
- Savage, S., Dai, R., 1993. Studies of granular shear flows wall slip velocities, 'layering' and self-diffusion. *Mech. Mater.* 16 (1–2), 225–238.
- Savage, S.B., Hutter, K., 1989. The motion of a finite mass of granular material down a rough incline. *J. Fluid Mech.* 199, 177–215.
- Su, X., Xia, X., Liang, Q., Hou, J., 2022. A coupled discrete element and depth-averaged model for dynamic simulation of flow-like landslides. *Comput. Geotech.* 141, 104537.
- Viroulet, S., Baker, J., Edwards, A., Johnson, C.G., Gjaltema, C., Clavel, P., Gray, J., 2017. Multiple solutions for granular flow over a smooth two-dimensional bump. *J. Fluid Mech.* 815, 77–116.
- Yan, X., Wen, J., 2020. Study on factors influencing the performance of reactive powder concrete. IOP Publishing.
- Yang, E., Bui, H.H., De Sterck, H., Nguyen, G.D., Bouazza, A., 2020. A scalable parallel computing SPH framework for predictions of geophysical granular flows. *Comput. Geotech.* 121, 103474.
- Zhang, Y., Campbell, C.S., 1992. The interface between fluid-like and solid-like behaviour in two-dimensional granular flows. *J. Fluid Mech.* 237, 541–568.
- Zhou, G.G., Du, J., Song, D., Choi, C.E., Hu, H., Jiang, C., 2020. Numerical study of granular debris flow run-up against slit dams by discrete element method. *Landslides* 17 (3), 585–595.
- Zhou, G.G., Li, S., Song, D., Choi, C.E., Chen, X., 2019. Depositional mechanisms and morphology of debris flow: physical modelling. *Landslides* 16 (2), 315–332.